Comparison of Characterization Methods for CdTe/ CdZnTe Radiation Detector Materials and Development of an Automated Test System

Alexander Winkler

born on 20.12.1983 in Eisenach, Germany

Physikalisch-Astronomische-Fakultät

Friedrich-Schiller-Universität-Jena

Submitted on:

27th May 2011, Jena

This page is intentionally left blank

Supervisor:	Ph.D. Tom Schulman Sensor Center Ltd.
1. Reviewer:	Prof. Dr. rer. nat. Carsten Ronning Institute for Solid State Physics University of Jena
2. Reviewer:	Prof. Ph.D. Risto Orava Helsinki Institute of Physics University of Helsinki

Day of diploma awarding:

This page is intentionally left blank

This work is dedicated to my grandmother who always wished that someone in the family will become a Doctoral student. With this thesis the possibility arises to follow that path and at the same time will be the first step on it.

Acknowledgements

For the possibility of writing a diploma thesis not only at an external institution, but also at foreign university I wish to thank Prof. Dr. Carsten Ronning and Ms. Hanna Oberheidtmann from the University of Jena for their great support. Additionally I would like to thank Prof. Ph.D. Risto Orava from the University of Helsinki, who asked me to conduct the studies here in Finland and kindly provided me with equal support on the Finnish side.

From the staff of Sensor Center I would like to thank Tom Schulman for his generous scientific supervision, his constant open ear for problems and his cooperativeness. Juha Petäjäjärvi for the help with the coding for all the technical devices that were used and the integrating of all the bits and pieces into a program one can work with. Mike Anderson for the silent acceptance of the many broken crystals and devices. Anu Orava for her help at the last minute as well as the remaining staff for their support and openness to discussions.

At the University of Helsinki and the Helsinki Institute of Physics I would like to thank Rauno Lauhakangas for all matters on electronic devices and software we built together as well as the repair of a broken pre-amplifier. Thank you to Eija Tuominen and Esa Tuovinen for the organization and assistance of the 4-probe measurements.

In Jena my thanks go to Daniel Weigel, Dr. Kießling, Ms. Lüdge from the Institute of Applied Optics and Christian Karras from the Institute of Photonic Technology for providing the chance to build a simple prototype for the proof of principle as well as their advice for purchasing the correct components which saved a lot of time and money. Furthermore, my thanks go to Mattes Liebsch and Fabian Stutzki who invested a lot of time to find the most serious mistakes in grammar and language of this work.

At the Institute for Single Crystals in Kharkov, Ukraine I thank Ph.D. Dmitry P. Nalivaiko for the very fruitful discussions and the help in interpreting my data.

I thank my friend Karol Schober from the Aalto University School of Science and Technology for helping me to understand Matlab and providing useful suggestions to realize my ideas.

Finally I wish to thank my family and friends for their never ending support on my long journey of studies and for providing me with the possibility to follow this path.

This page is intentionally left blank

Contents

This page is intentionally left blank

List of Figures

LIST OF FIGURES

This page is intentionally left blank

List of Tables

Acronyms

Am-241 Americium-241

CCD Charge-coupled device

Cd Cadmium

Cs-137 Cesium-137

CT CdTe

CZT CdZnTe

FWHM Full width at half maximum

I Current

IR Infrared spectrum (electromagnetic radiation)

MCA Multi-channel analyzer

NA Numerical aperture

R Resistance

ρ Resistivity

σ Conductivity

Si Silicon

S/N Signal to noise ratio

Te Tellurium

TlBr Thallium (I) Bromide

UV Ultraviolet spectrum (electromagnetic radiation)

V Voltage

VIS Visible spectrum (electromagnetic radiation)

Z Impedance

Zn Zinc

1

Introduction

Radiation and its effects on humans and the environment is a serious topic concerning our modern civilization. The catastrophic consequences of failures of nuclear energy technology such as in Chernobyl, Ukraine in 1986 concerns generations. Natural disasters like earthquakes and their effects on nuclear energy facilities such as Fukushima, Japan teach us how dangerous the invisible threat of radiation can be.

Visualizing these threats is of substantial importance for decision makers, evacuation and health personnel, civilians and most importantly for workers at the sites of these accidents.

The visualization of ionizing radiation is challenging. Gaseous detectors such as the well known Geiger-counters have limited usage and efficiency, and they can detect only certain kinds of radiation. During a nuclear catastrophe all kinds of radiation is emitted, and a number of devices are required to obtain adequate information.

To increase the detector efficiency and to improve their usage, the research of the last decades has concentrated on solid state detectors. A higher atomic number yields higher quantum efficiency of a detection due to a higher interaction probability. Additionally, processing techniques common in semiconductor industries enable the creation of directionality sensors with spectroscopic capabilities. Furthermore, the devices can be miniaturized and packed into compact integrated units which can operate unsupervised and communicate with the latest standards (mobile, wireless network, etc.).

Many semiconductors are capable of detecting radiation, but only a few have a band gap sufficiently large enough to allow operations at room temperatures. Out of these, many materials are unsuitable for practical applications, such as TlBr which is highly

toxic and hygroscopic, or are subject to strong radiation damages (Si). Due to these circumstances, the most promising candidates are detector crystals made of CdTe (CT) and CdZnTe (CZT). This work focusses on the latter material, but most results apply similarly to CdTe.

Due to their capability to capture a wide range of gamma radiation and X-rays at room temperatures, CT/ CZT are of high interest for research and industry. High-energy, detector physics and material sciences are the largest fields in research, while material, medical and security industries are the driving commercial forces.
In research the most significant difficulty is that the growth process of CT/ CZT is still not fully understood. Additionally, several growth methods such as the high pressure Bridgman method (and adaptations of it) or travelling heater method are fragmenting the understanding further.
Growing detector grade material is still treated more as an art instead of a reliable science. Even established research institutions[1] with many years of experience of growing the material still have problems in reproducing similar crystals for identical growth conditions. Therefore, it is most important for the research to gain access to crystals characterization data which is as detailed as possible. However, the characterization methods available are neither very detailed nor suitable for testing large numbers of crystals, which are needed for reliable statistical data. Additionally, only little attention has been given to on the comparison of characterization data from different methods to understand effects. The whole field of research is still at its beginning.
Because the growth process is not understood very well the industrial scale production for these materials is also problematic. Currently there are only a few big suppliers[2] that can produce CT/ CZT detectors in large quantities. The production process is costly due to the low yield of the growth process. Each crystal has to pass through the whole production cycle and must be tested intensively, which is a time and resource consuming process, and in addition many detector crystals turn out to be of low quality and have to be thrown away. To ease these uneconomical situations, the producers define their own quality standards and tests to best fit their products. In conclusion this leaves a scattered definition of the quality throughout the industry and embarrasses the customer in finding the right solution for the application in mind. Each application

[1] Such as ISC, Ukraine [35] with more than 15 years of experience.
[2] AcroRad/ AcroTec, Eurorad, eV Products, Orbotech (GE), RedLen

requires a different grade of crystal. Detection is less demanding than imaging which is inferior to directionality and spectroscopic purposes.

To summarise all from the above the understanding of the growth process of CT/ CZT is of substantial value for research and industry to improve processes, products and to establish quality standards. This can only be achieved by detailed characterization and investigation of the grown material.

Therefore, the first goal of this work is to develop an automated test system that acquires data of CT/ CZT crystals by several different test methods and under comparable conditions. The acquired data are to be compared to results from established test methods and patterns are searched for. Lastly an evaluation of the practicability in a production environment will be done.

Some test methods have the capability to provide data for one or many single tests. Therefore, the next goal of this work is to simplify the characterization process by combining and replacing tests.

As stated above a major problem of industry, customers and research is the lack of definition standards, which criteria does a crystal need to fulfill to be able to be used as a spectrometric detector. For this reason another aim of this work is to find possible candidates for such criteria.

One of the first ideas of this work was to develop a test system that can test a crystal not only with precision and automation, but also in as many ways as possible in an early stage of production. With the data obtained, an approximation of the crystal's performance as a detector can be made. However, to be able to make such a prediction, an organized statistics of as many crystals as possible are needed. Another aim of this work is the development of a CT/ CZT crystal characterization database and to suggest what information it should contain.

The primary goal is the development of an automated test system. Therefore, the structure of this work is adjusted to support this objective. In Chapter 2 the most important physical fundamentals, needed for the understanding of the function and performance of solid state radiation detectors, are explained. The actual chosen methods of testing and their detailed description will follow in Chapter 3. Since the focus

of this work is on the comparison of several test methods, the data produced by each test are collected in Chapter 4 and are not presented together with the results and discussion of these. Chapter 5 deals with this matter. Finally, Chapter 6 will summarize the obtained results and discuss the set aims of this work. Additionally Chapter 6 will provide an outlook for further research that with the results of this work, will gain attraction. To complement the topic of radiation, a brief description of radiation and safety instructions is added to Appendix A.
Each chapter also includes a short introduction and summary of it, as it is customary in theses in Germany. Although, it is not customary at the University of Helsinki, but this thesis is to be submitted at the University of Jena, Germany and thus the local standards are respected.

2

Fundamentals of Detector Crystal Characterization

This chapter will provide an overview on the theoretical fundamentals needed to understand the functionality of solid state radiation detectors and the methods to test such devices. Because of the numerous fields of physics utilized for several test methods, it will not be possible to cover each field completely. Therefore the focus is put on the actual physical effect exploited to measure certain properties.
The division is made into three larger sections: electrical and optical properties as well as detector theory. Each covers the main aspects needed to understand the chosen test methods of Chapter 3.

2.1 Resistivity Measurements

The resistivity ρ is an important characteristic of a semiconductor as it is crucial for the material's performance as a detector (diode).
Resistivity depends on the free electron and hole densities (n, p) as well as their mobilities μ_n and μ_p and is defined as specified in [1]

$$\rho = \frac{1}{q(n\mu_n + p\mu_p)} \tag{2.1}$$

where q is the elementary charge. In extrinsic materials the carrier majority is much greater than the carrier minority, the latter of which can be neglected. The practical

implementation of measuring the charge densities and mobilities is a nontrivial task established by the approach of measuring the resistance.

2 and 4 point measurements

The main difference between 2 and 4-probe measurement [1] is that in the second the current and voltage are measured through separate probes in the correct electronic way (*german: spannungs-/stromrichtig*). While both are done over the same electrodes in the 2-probe method, Figure 2.1. There the resistance R is measured as a series of the partial resistances of the wires (including needles) R_W, contacts R_C and the actual object R_O resulting in the total resistance R_T of the system. For the 4-probe method, R_W and R_C can be neglected due to the high input impedance Z of the voltage meter and therefore the low current in that path, so basically only R_O is measured.

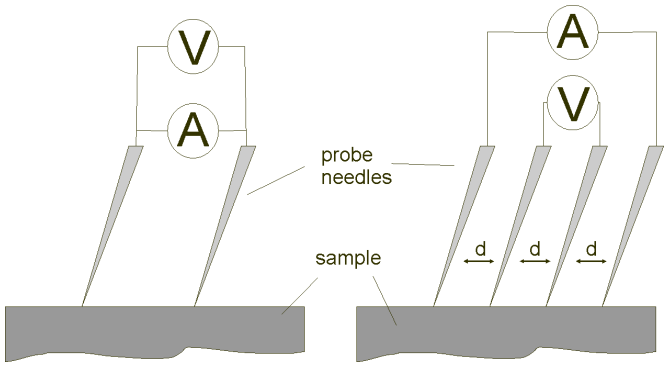

Figure 2.1: Schematic drawing of a 2 and 4-probe resistivity measurement. - *A, V* are ampere- and voltage meters. The 4-probe method uses electrodes for each device separately. For that method the probe needles are kept at constant equal spaces which simplifies the measurement.

$$R_T = 2R_W + 2R_C + R_O = \frac{V}{I} \tag{2.2}$$

The resistivity ρ is a value that also takes some of the material's physical properties into account and provides the resistance R as a function of the area A and thickness d

$$\rho_{general} = R \cdot \frac{A}{d} \tag{2.3}$$

with the surface area perpendicular to the electric flow and the thickness of the sample. As derived in [1], the resistivity of the 4-probe method with special needle spacing

reduces to

$$\rho_{4-probe} = F \cdot \frac{V}{I} \tag{2.4}$$

with F as corresponds to a correction factor accounting object size, minority carrier injection, high resistance, temperature, etc.

By utilizing these methods, one can obtain resistivity values for about any material. However, two systematic problems will still occur. Firstly, in case of two side measurements (an electrode on each side of the crystal, 2-probe method only), one has to ensure that the contacts are ohmic. The resistance of the bulk material can be only measured this way. Secondly, it must be ensured that the used needles will cause only little damage to the surface of the crystals. This second problem can be resolved by using temporary contacts (e.g. mercury, however it is environmentally dangerous and toxic, hence no practicable option) or a contactless resistivity method.

2.2 Optical Characterization

This section provides an overview of the different optical aspects needed to follow the function of the optical tests. The beginning is done by geometric optics with the explanation why microscopy can be used to scan a sample in 3 dimensions (3D). This is followed by an outline of which (image) resolution is of reasonable usage. Next, an excursus to solid state physics will explain the transparency of the materials (Cd, Zn and Te) as well as their absorption behaviours. Both can be used for characterization of the raw materials and their compounds. Finally, the functionality and effects of semiconductor detector physics are outlined.

2.2.1 Microscopy Theory

Focal area

The basic functions of a microscope are described in [2], [3] and will not be explained at this point. Nonetheless, the reason why such a device can be used only to gain information of a certain area is explained below.
Because the second lens system (ocular) of a microscope magnifies a real image of the first system (objective), the overall magnification M is the multiplication of the

contributing factors $M_{objective}$ and M_{ocular} of objective and ocular

$$M = M_{objective} \cdot M_{ocular} \tag{2.5}$$

The magnification factor in general $M_{general}$ is defined with

$$M_{general} = -\frac{x'}{f} \tag{2.6}$$

with x' the distance from the focal point to the image on the picture side and f the focal length of the lens. To keep M constant in a microscope the distance between ocular and objective is kept constant and called tube length (160 or 254 mm). It is the sum of the distance from the focal point of the objective to the focal point of the ocular. There the first one is on the picture-side and the second one on the image-side of the referring device. (See Figure 2.2, drawn according to [2].) As a result of this only objects that are positioned within the focal area of a microscope are seen sharply. For this reason, other objects do not interfere with the objects in the focal area.
The main reason for this is that in both cases, when the object is either before (Figure

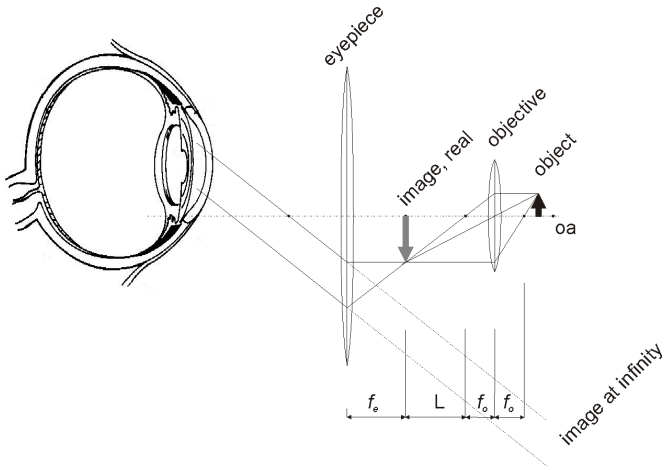

Figure 2.2: Ray diagram of the optical path in a microscope. - ao - optical axis, f_e - focal distance eyepiece, f_o - focal distance objective, L - tube length.

2.3) or behind (Figure 2.4) the focal area of the objective, a real image will be produced outside the first focal point of the eyepiece, a real image that can only be seen on a screen. Therefore, a following camera (or observer's eye) will again convert the image to a virtual one and project it on the CCD (retina). Especially microscope cameras are

not able to project information that originated outside the focal area of the objective to the CCD, because their fixed focal ranges are designed to project an virtual image from infinity to a CCD, only.

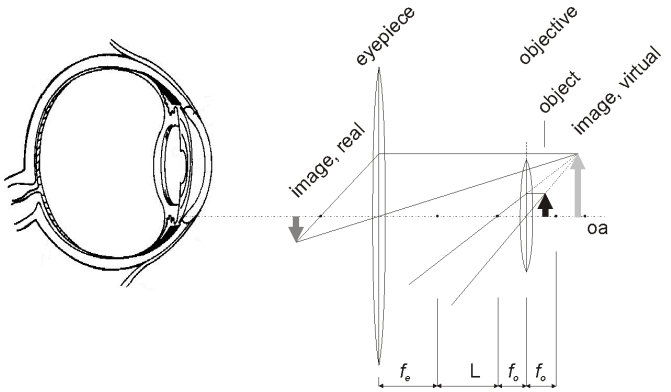

Figure 2.3: Ray diagram for the case where the object is in front of the first focal point of the objective - A real image is produced after the eyepiece that can only be seen on a screen, but not with a camera or by an observer.
ao - optical axis, f_e - focal distance eyepiece, f_o - focal distance objective, L - tube length.

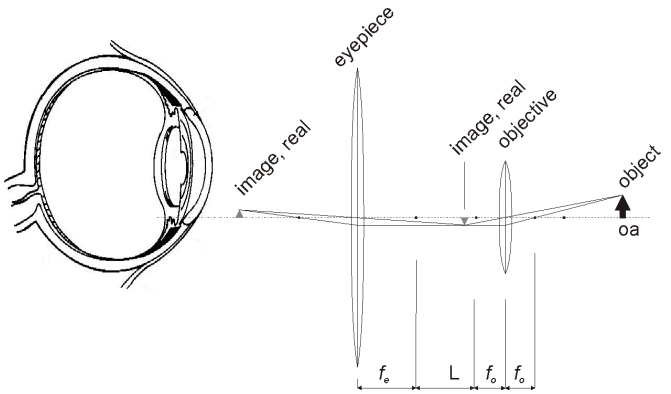

Figure 2.4: Ray diagram for the case where the object is behind the focal area of the microscope. - Again a real image is produced after the eyepiece, which can only be seen on a screen, not on a CCD or eyepiece.
ao - optical axis, f_e - focal distance eyepiece, f_o - focal distance objective, L - tube length.

Image resolution

The resolution of a recorded microscope image is limited by several factors such as optical restrictions, resolution of the capture device and the wavelength used. Each of these factors will contribute to the final image resolution.

According to [3] the resolution of a microscope is defined by the relation below.

$$\Delta x_{min} = 1.22 \cdot \frac{\lambda}{2n \cdot \sin\alpha} \tag{2.7}$$

With Δx_{min} as the given minimal distance of two distinguishable points. It is therefore the maximum resolution of the system. λ is the wavelength, n the refractive index of the medium between the objective and the object and $\sin\alpha$ half of the opening angle of the used objective, while $n \cdot \sin\alpha$ is defined as the numerical aperture NA. The second lens system (eyepiece) in a microscope has similar characteristics. However, since the purpose of the eyepiece is to enlarge a picture of the objective, the actual limiting factor is set by the objective. Relation (2.7) already takes into account the wavelength used. The resolution of the capture device R_{cam} (assuming all optics are accounted in the microscope) is the pixel size (area) of the capturing chip, and is usually given in μm.

The final resolution R_f of all components is the product of all partial resolutions, and is dominated by the smallest contributor. $R_f = R_{cam} \cdot \Delta x_{min}$. For the used components (microscope $NA = 0.45$, pixel size camera = 3.6 μm, wavelength used = 875 nm until 2750 nm) this will be for the upper limit:

$$R_{f,\,up} = \left[3.6 \left(1.22 \cdot \frac{2.75}{2 \cdot 0.45}\right) \frac{1}{3.73}\right] \ \mu m = 3.59\,\mu m$$

and for the lower limit of the spectra.

$$R_{f,\,low} = \left[3.6 \left(1.22 \cdot \frac{0.875}{2 \cdot 0.45}\right) \frac{1}{3.6}\right] \ \mu m = 1.52\,\mu m$$

As a result of this equation the chosen camera resolution is too small for the complete spectral interval and will only resolve structures above $\approx 3.6\,\mu$m. However, due to the fact that the average defect size is of several μm is this camera an acceptable compromise.

2.2.2 Transmission of the Component Materials

The reflectivity $R(\omega)$ is given by the Fresnel-relation for perpendicular incidence. With ω the angular frequency of the used electromagnetic radiation and neglecting of scat-

tering processes; equation (2.8).

$$R(\omega) = \left| \frac{\sqrt{\varepsilon(\omega)} - 1}{\sqrt{\varepsilon(\omega)} + 1} \right|^2 \tag{2.8}$$

Here $\sqrt{\varepsilon(\omega)}$ is the general complex refraction index[1] for the material and takes absorption processes into account. Assuming the relation is also valid for transition metals such as Cd and Zn, the refraction index is provided by the square root of the Drude-relation for the complex dielectric function [24].

$$\varepsilon(\omega) = 1 - \frac{\omega_p^2}{\omega(\omega + \frac{i}{\tau})} \tag{2.9}$$

With τ the electrons mean free time between ionic collisions, and ω_p the plasma frequency for the material. In case of optical frequencies ($\omega \approx 10^{15}\, s^{-1} < \omega_p$; damping coefficient $\omega\tau > 1$) the dielectric function is approximated by

$$\sqrt{\varepsilon(\omega)} \approx \frac{\omega_p}{\omega} i \tag{2.10}$$

which results in $R(\omega) = 1$ for many metals within UV and VIS, but differs by entering the IR spectra. With values of Cd [8], Zn [7] and Te [14] in relation (2.10) and (2.8), one obtains the reflectivity values for these elements at 1.31 eV ($\lambda = 950\,\text{nm}$). The spectra of Te for example is shown in Figure 2.5. The transmission T and reflectivity

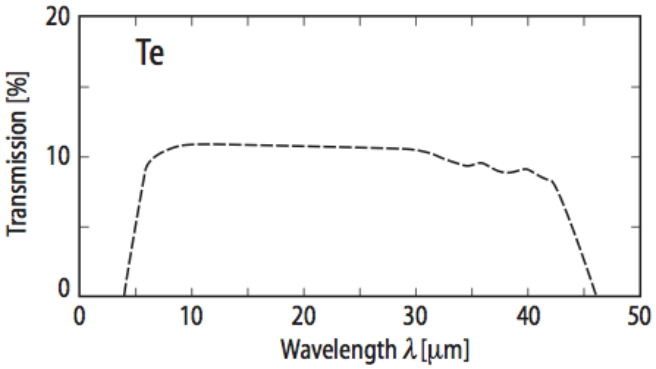

Figure 2.5: Infrared transmission spectrum of Tellurium. - The transmission has no significant value until $\lambda \approx 4\,\mu$m. Before that the reflectivity is nearly 1, which results in dark spots an IR image. Graph from [9]

[1]The refractive index $\sqrt{\varepsilon(\omega)}$ is more commonly referred with $n(\omega) = n(\lambda)$.

R are connected via the relation (2.11) below.

$$T = \frac{(1-R)^2\, e^{-\alpha\, d}}{1 - R^2\, e^{-2\alpha\, d}} \tag{2.11}$$

Whereas d the samples thickness is and $\alpha = \alpha(\lambda)$ the absorption coefficient for that material. As derived in [11], the absorption coefficient for the infrared region can be assumed to be 0, which reduces relation (2.11) to

$$T = \frac{(1-R)^2}{1-R^2} \tag{2.12}$$

by inducing an error of less than 1 %. According to the equations (2.8), (2.10) and footnote 1, the reflectivity R can be written as

$$R = \frac{(n(\lambda)-1)^2}{(n(\lambda)+1)^2}\,. \tag{2.13}$$

Applying the relations above for CZT (numbers from [10]), one will receive a reflectivity of 21 % and a transmission of 65 % which is comparable to the 66 % estimated by Sen, et al. ([11], or [12] and [16]). The remaining 14 % are due to reflective losses on the second surface of the crystal and its iterations. Passing light is not only reflected on the first surface, but also on the second surface when exiting the crystal into the air. Also, reflections and transmissions on the internal surfaces contribute to losses and transmissions, which leads to the overall transmission of $\approx$ 65 %.

2.2.3 Constance of the Refractive Index

With the theory above, the frequency dependent refractive index $\sqrt{\varepsilon(\omega)} = n(\omega)$ was introduced. This complex number, due to its imaginary part, varies with the energy (spectral range) and the concentration of Zn. In shorter intervals however, the variation is small and can be deemed to be constant. For Cd and Zn this results in a reflectivity of less than 33 % respectively 41 % within the chosen energy of 1.41 ... 0.45 eV (875 - 2750 nm).

In the compound semiconductor CZT, the refractive index $n(\omega)$ can vary more strongly (2.70 to 2.94) with a changing concentration of Zn [10], but will become more leveled for all concentrations around $n(\omega) = 2.65$ in the mid- and far-IR region.

Applying relation (2.10) with the numbers (from [10]) for x = 0.1 in $Cd_{1-x}Zn_xTe$,

the refractive index $n(\omega)$ calculates to 2.76 over the full region of interest. Variations occur only in the 6th position after the comma, which is constant enough for all further calculations. This calculated number is in very good agreement with the experimental results obtained during the IRM test, (Chapter 3.1.2), in which the optical path within a crystal is contracted and therefore so is the movement in that direction.

Due to the little variances of $n(\omega)$ over the chosen spectral range (875 - 2750 nm) the reflectivity and therefore the IR transmission is the only varying argument, which is why this method can be used to produce a relative Te density map of a crystal. This approach is pursued for the IRS test method in Chapter 3.1.2.

2.3 Detector Theory

High energy radiation produced from nuclear decays, cosmic radiation or in particle accelerators are detected by so called radiation detectors. There are several kinds of detectors based on different effects of physics which are used for specialized tasks (detection of momentum, spin, charge, energy, etc.).
The most common detection principles are based on ionization and scintillating effects, but more unusual principles like Cherenkov-light are also used today. This work will focused on solid state semiconductor detectors.

2.3.1 Semiconductor Detectors

There are several advantages to semiconductor detectors in comparison to other kinds such as gaseous detectors. A few of them are:

- the band gap of the material can be engineered with its doping concentration and thus the ability to detect a certain energy range of radiation (e.g. hard or soft X-rays)
- the energy needed to create an electron-hole pair is small in comparison to gas (about 1/10), which is the reason for achieving a better energy resolution
- solid state materials have a high specific density, and small and self-supported devices can be produced in high numbers

- industrial techniques from chip electronics can be used to reduce costs and increase quality, energy- and spatial resolution
- charge carrier density and mobility is higher than in gases (see Table 2.1 below for detector grade Si at 300 K)

Table 2.1: Comparison of charge properties for semiconductor and gas detectors - Number of charge carriers n, p (electrons, holes) and their mobilities $\mu_{electron}$, μ_{holes}. The number of carriers is also the doping intensity. *Charge multiplication has been taken into account for gas detectors, all values for Si at room temperatures.*

	Semiconductor	**Gas**
n (cm^{-3})	10^{12}	$10^2 - 10^4$
p (cm^{-3})	10^{15}	$10^2 - 10^4$
$\mu_{electron}$ $\mathrm{cm}^2/\mathrm{Vs}$	1350	10^3
μ_{hole} $\mathrm{cm}^2/\mathrm{Vs}$	450	10

2.3.2 Charge Carriers and Band Structure

Judging by the energy band gap semiconductors are positioned between the band overlapping metals and the big gaps of isolators, as outlined in Figure 2.6. Materials

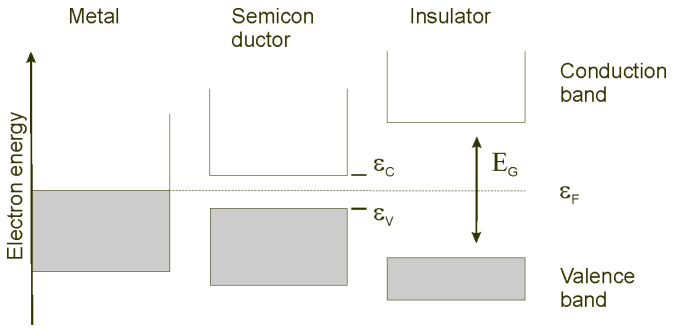

Figure 2.6: Energy band structure of metals, semiconductors and insulators. - ε are the energy levels of the conductive band, Fermi-energy and valence band and E_G is the amount size of the gap between valence and conductive band. Drawn according to [24].

with band gaps of around 1 eV are usually considered to be semi- or hot conductors since the thermal energy can excite electrons into the first unoccupied (conduction) band. The thermal energy at room temperature (≈ 26 meV) can excite electrons into the conduction band as well, but is statistically negligible.

In the case of being excited, the electron has a higher degree of freedom to move across

the crystal structure which can be forced with an electric field applied. Furthermore, each excited electron leaves a vacancy in the last occupied energy (valence-) band of the material. These vacancies are referred to as holes and will move similarly to a positive charge in an electric field. In the case of a detector this flow of electron-hole pairs will then represent the signal one intends to measure.
The applied field is also responsible for the charge carrier drift velocity $\nu_{n,p} = \mu_{n,p}E$. This velocity is proportional to the field and can reach up to 10^5 m/s, which corresponds to a time of 10 ns per mm [5] and is sufficiently fast for most applications.

The number of charge carriers in a pure semiconductor is too small for efficient signal collection. One way to increase that number would be to reduce the band gap close to the Fermi-level, but this also increases the thermally generated *n, p*-pairs, hence the noise. The ideal material should have a large band gap, but its charge carriers a small excitation energy only. This problem is solved by inducing energy levels close to either conduction or the valence band, which is achieved by doping the semiconductor with a material that has a different number of valence electrons, such as the elements of the semiconductor's neighbouring groups in the periodic table. In case of *Si* these materials are for example boron and phosphor. Boron as a dopant misses an electron (hole, *p*, acceptor) in an electronic bond which makes that region acceptable for an electron to fill. Therefore, these materials are called *p*-type semiconductors since the charge carrier majority are holes. In contrast as a dopant has phosphor one electron (*n*, donor) too many at its electron bond, which will easily be excited into the conductive band and represents the majority of charge carriers in *n*-type semiconductors.
From these energy levels the needed charge carriers can now be exited more easily, which increases the conductivity sufficiently for an effective signal transport (see Figure 2.7).

2.3.3 Functionality and Signal Degradation

By combining a *n*- and *p*-type semiconductor (e.g. via vapour deposition) a junction is created which combines the regions of donor and acceptor abundances. A net flow of either one into the region of the other will start to recombine electrons with holes. A

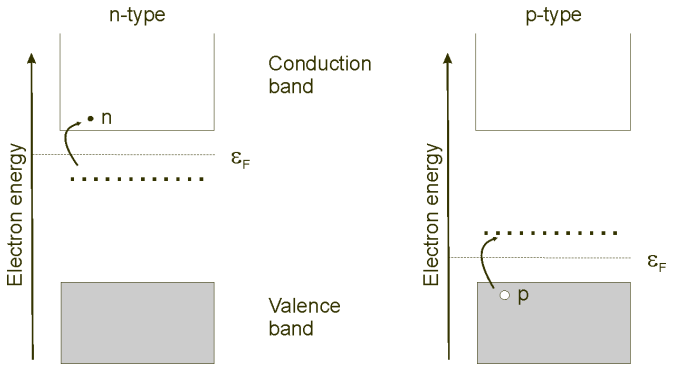

Figure 2.7: Energy band structure of *n*- and *p*-type doped semiconductors. - ε_F is the Fermi-energy; n, p are donors and acceptors. Drawn according to [23].

charge build up in an area causes a potential which is described by the Poisson equation

$$\Delta\varphi(\mathbf{r}) = \frac{\rho(\mathbf{r})}{\epsilon_0\epsilon_r} \tag{2.14}$$

with ρ the charge distribution profile and $\epsilon_0\epsilon_r$ the permittivity. By integrating equation (2.14) the potentials shape is found (see Figure 2.8). In stationary (- ceased net flux) the potential difference across the junction is about as big as the band gap of the material, and the direction of the potential hinders further charge carriers to enter the region. From the difference in potential the statical electrical field $\mathbf{E}(\mathbf{r})$ can be derived from Maxwell's equations. $\mathbf{E}(\mathbf{r})$ extends over the size of the depletion region. The fields gradient and shape is also shown in the Figure 2.8. And $\mathbf{E}(\mathbf{r})$ will prevent electrons and holes from entering the region as well as pushing them back to the n, p regions they originate from. This effect leads to the term *depletion layer* and a high resistance of it. Any new generated (e.g. by radiation) electron-hole pair will also be pushed out of the region. Their movement causes the signal one intends to measure. Therefore, the *depletion layer* is the active region where the process of detection occurs.

The phrase 'ionizing particle' indicates the process of interest. A high energetic particle that passes through the depletion layer will loose its energy by creating electron-hole pairs along its path, by the means of photoelectric absorption. These can create further pairs, but the overall number of pairs is constant for a certain energy of the particle and the material. This makes it possible to record energy spectra that refer to the spectra of the indicating radiation under the assumption that the particle is completely

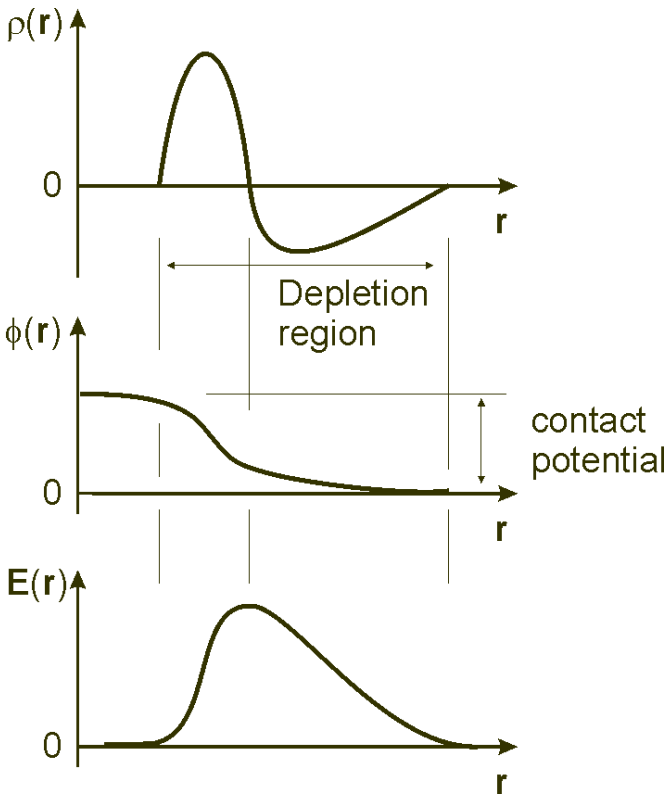

Figure 2.8: Schematic drawing of the charge distribution profile $\rho(\mathbf{r})$, electric potential $\varphi(\mathbf{r})$ and electric field $\mathbf{E}(\mathbf{r})$ across a *pn*-junction. - The left side is doped with donors n and right side with acceptors p. Drawn according to [5].

stopped within the detector.
The energy needed to create one electron-hole pair is called *ionization-energy* ϵ, following the nomenclature used for gas detectors. In semiconductor detectors, this ionization energy is only $1/10$ (3 eV) of the energy needed in gas detectors to create such a pair, which is the reason for the better energy resolution of these kind of detectors.

An applied field of several (hundred) volts is needed for the created charge carrier pairs to travel to their electrodes. However, since the material has a finite conductivity some current will always be flowing. This flux is called a *leakage current* and is a function of the electrode material, their position and configuration, the material's resistivity and for high resistive materials ($> 10^7\,\Omega/\,\mathrm{m}$ = CZT) also of the surface condition. This makes the reduction of the leakage current an important part in achieving good signal to noise ratios (*S/N*), which are needed for better detection performance.

A formed electron-hole pair has a theoretical lifetime of up to a second [5], but in practice much shorter lifetimes like $10^{-3} \ldots 10^{-5}$ s are observed. These reductions are mainly due to remaining impurities in the crystal's lattice that induce new energy levels inside the band gap of the semiconductor. These levels are called deep impurities and act as traps for the pairs. Even if the charge carrier is immediately released (but can be trapped longer) the time for that process takes longer than the average collection time of the originally created charge cloud. The carriers released from deep traps can still be collected, which results in a peak broadening (increasing of FWHM), and if numerous enough also in ghost signals; both are highly unwanted in detection applications. For this reason the process of deep impurities is also called *deep charge trapping*.
Another reason for the reduction of the carrier lifetime are recombination centres which can capture both electron and hole (shortly after another), recombine them and be able to capture new carriers again. These centres are the main reason for recombination within a crystal because the energy needed for an electron/ hole to be excited into the recombination center is smaller (and therefore more probable) than the energy needed to cross the complete band gap for a recombination process.
Besides material impurities, flaws in the crystal's lattice can induce further trapping and recombination centres. These flaws can be anything from point defects to bulk defects which is one reason for the need of a single crystal material for detector applications.

2.3.4 Operation of a Detector

A detector with a plain *pn*-junction is only a poor radiation sensor, since thickness of the 'active' layer is very thin and the carrier speed very low. By applying an external voltage both aspects can be improved. The junction, which is basically a diode, has the property of a conducting current in one direction (*forward*) easily while blocking the other one (*reverse direction*). In case of a positive bias voltage applied on the *p*-side, the changed potential (see Figure 2.9) will now more strongly attract electrons towards the *p*-side and vice versa, because each carrier majority has less potential to overcome. Thus a high conductivity for this set up is achieved.
In case of applying reversed bias polarity to the junction (negative voltage on the *p*-

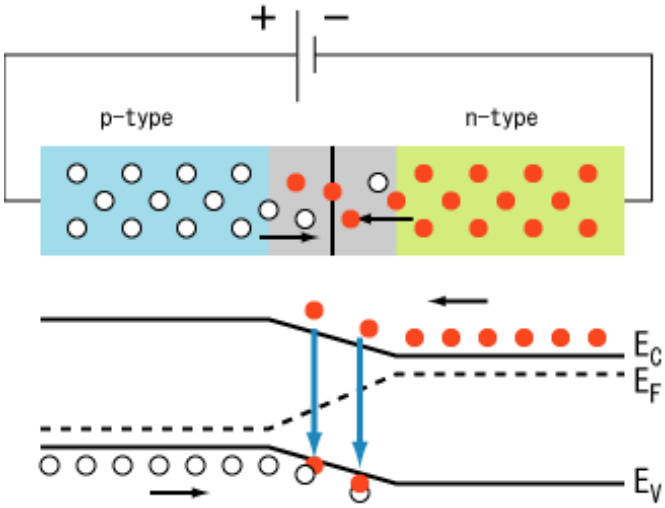

Figure 2.9: A *pn*-junction in forward bias. - The charge carriers (*n*,*p*) of each side are attracted towards the depletion region, which increases the conductivity. Underneath the change of energy levels. Depicting the forward bias lowers the step each carrier has to manage to reach the other electrode. Image taken from [28]

side), the potential to cross the junction is increased and is therefore less probable due to the higher energy needed to overcome the potential-step (Figure 2.10). Only carrier minorities (electrons on the *p*-side, holes on the *n*-side) are encouraged to travel. Because their number is much smaller, the current over the junction is much smaller (and part of the leakage current). This behaviour is similar to the one of a rectifier used as a discriminator.
If the reversed bias voltage is increased high enough the depletion region can be in-

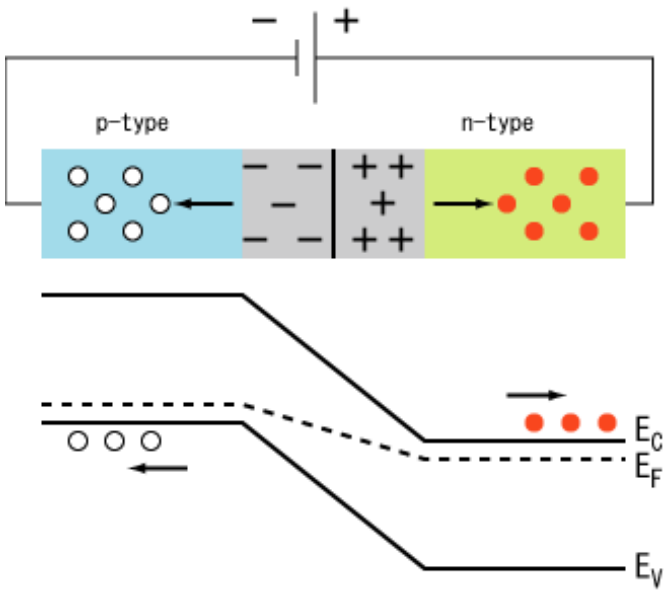

Figure 2.10: A *pn*-junction in reverse bias. - The charge carriers (n,p) of each side are repelled from the depletion region, which decreases the conductivity. Underneath the change of energy levels. Depicting the reverse bias increases the step each carrier has to manage in order to reach the other electrode. Image taken from [29]

creased over the full thickness of the bulk material, which will lead to better signal capture, saturated charge mobility and higher signal to noise ratios. It is problematic however, that the full depletion voltage is usually close to the breakdown voltage, which can permanently destroy the junction and physically damage the crystal.

2.3.5 CdZnTe Detectors

Most semiconductor detectors are made from Si or germanium and their compound structures. A rather young candidate for room temperature detection in this field is CZT. These crystals are a solid solution of ZnTe in CT to combine the good γ-absorption efficiency of CT with the high resistivity of ZnTe [1], but without polarization effects as they are found for CT. The blend factor x provides the ratio of the solid solution in the compound material $Cd_{1-x}Zn_xTe$ and is usually set between 0.1 ...0.2 for detector applications. Thus these CZT compounds have a band gap of 1.57 ...1.64 eV [5, 20]. Another interesting aspect is the charge carrier mobility which differs strongly from $\mu_n \approx 1350\,\mathrm{cm}^2/\mathrm{Vs}$ for electrons and $\mu_p \approx 120\,\mathrm{cm}^2/\mathrm{Vs}$ for holes in these materials. Due

[1] Though Zn was originally added to improve the electrode application.

to their speed the electrons are usually the choice for charge capture.
The material is mostly grown by variations of the unseeded high pressure Bridgman method, but the process is still after more then 30 years of research not completely understood. Defects such as metal inclusions/ precitipates[1], grain boundaries, grains, polycristalinity and uneven raw/ doping material distribution are major problems. These problems lead to an intensive and costly process of characterizing and choosing detector grade parts of a grown ingot and makes most of the costs of commercially available CZT detectors. This work concentrates on this problem and aims to improve the situation. If a suitable detector is found, then the performance is usually superior to other available devices at room temperature that clean spectra with high S/N ratios can be acquired, (Figure 2.11).
Hole trapping, due to their low mobility μ_n, reducing the charge collection efficiency of

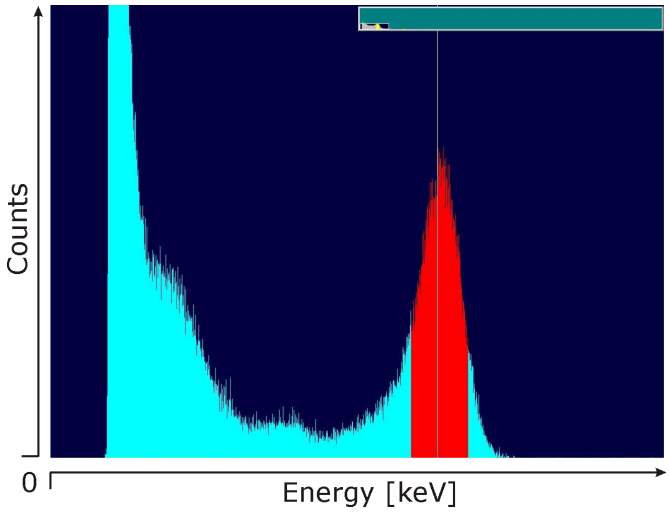

Figure 2.11: Spectrum of Am-241 source captured with a CZT detector of high resistivity and structural quality. - The red marked area is the 59.5 keV peak from the strongest γ-emission at a probability of 36%. The yellow bump on the right top side is the calibration peak at 178.5 keV = 3 x 59.5 keV.

CZT detectors and produces an asymmetric long tail in the measured spectra[2]. Several methods have been used in order to minimize this effect. Mostly the approach of single charge carrier sensing is used by which electrons only will be captured. This

[1] Precipitates are chemically nano/ micro-crystals within a single crystal structure, while inclusions are point defects such as impurity incorporation of other elements. For CZT defects it has been adopted to equate inclusions with precipitates.
[2] Referred to as 'hole tailing' in the literature.

can be achieved by using both electronic methods (pulse rise time discrimination and biparametric analysis) as well as careful electrode design (e.g. Frisch-grids [13], pixels, coplanar grids, strips, multiple electrodes). Another approach is the planar transverse field (PTF) technique in which the γ-irradiation is carried out in direction orthogonal to the applied electric field, but the signal interpretation is more difficult for this technique. These options have to be evaluated for each application separately.

Synopsis

We have seen in this chapter that, if approached with devices sensitive enough and basically the Ohm-law, the resistivity of highly complex structures such as compound materials can be determined. Geometric optics can explain why only the field of focus (nothing before and behind it) is projected to the observer, and the transparency to IR light for semiconductors (CT/ CZT) is based on the material's refractive index. Furthermore, the principle structure and functionality of solid state detectors is explained and how this can be used to convert ionizing radiation into a signal.

3

Chosen Methods and Final System

The major goal of this thesis is to build an automated test system with as many tests included as possible, not only to meet every vendor's standards, but also to compare the state of the art research, which is at least as scattered as the vendor's quality standards.

In the first stage of the research (this thesis), the focus is put on optical characterization (IRP, IRM, IRS) and the comparison to established test methods such as resistivity and γ-test. The next stage will add further tests for comparison such as contactless resistivity test, electrical field analysis and internal stress test.

Due to the fact that the test system was completely developed for this research, most components needed to be designed especially for the new applications. This design process was carried out with the prospect to include all test methods covered in this chapter, and to ensures that the integration of the remaining test methods will be a simple and fast task.

Tests included in the first stage will be described in detail in their function and realization, while the tests of the second stage as well, as their integration into the system, are mentioned briefly. The final system, after the first stage is presented in Figure 8.2 , Appendix B.

3.1 Test Methods of the First Stage

3.1.1 Resistivity Measurements

For resistivity measurements, the 2-probe method is chosen as an easy and fast test to find a semiconductor's ohmic resistivity. Unfortunately this can only be realized in a separate device. However, the characterization test system is designed to include contactless resistivity measurements which will be used in later studies to confirm the data taken with the 2-probe method.

The data is acquired with a probe station within a light tight box, such as can be seen in Figure 3.1. A crystal is placed on the conductive rubber with one electrode

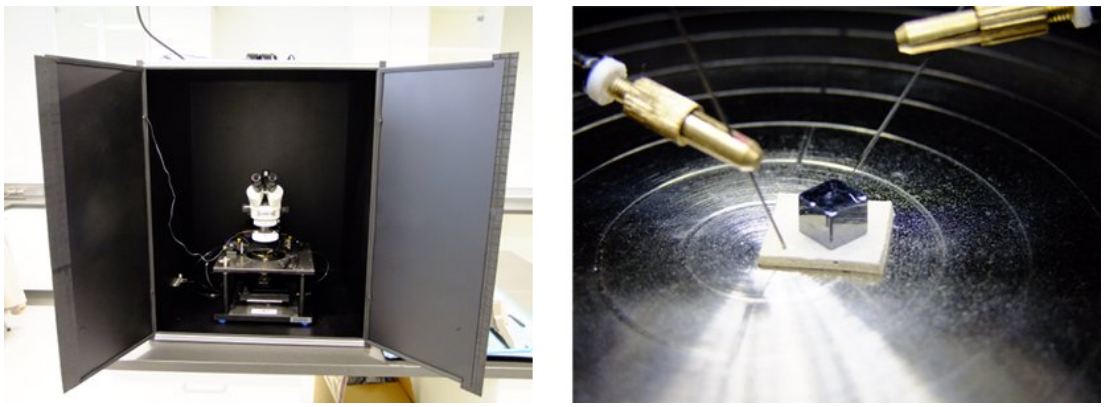

Figure 3.1: Probe station for the resistivity test. - Image of the whole station with the light tight box on the *left*. The main devices are the white microscope, micrometer table and the micrometer screws for the electrodes. The probe needles (electrodes) and a crystal are displayed on the *right* side.

of the probe station connected, while the other electrode is slowly placed (micrometer screws) on top of the sample (see Figure 8.1, Appendix B), to ensure a secure connection with the least possible surface damage. Afterwards, the light tight box is closed and a pause time of 30 minutes is kept to ensure that photogenerated charge carriers have completely discharged. In the next step a computer-controlled high voltage sweep (power supply: *Iseg DPR - 50 205 12 5*) is applied to the sample while its leakage current is continuously recorded with a *Keithley 6487 picoammeter*. The voltage sweep ranges from 0 V to maximum and back to 0 V. This is done to ensure that no permanent damage (such as breakdown) has occurred to the crystal.
The testing is done for both voltage polarities and both sides, and the polarity of the

best result is marked on the crystal on the side of its recoding. This information is needed for polarity depending applications the crystal might be used for.

3.1.2 Optical Characterization

The big advantage of optical characterizations is that they are fast and non-destructive, and the sample usually requires only a minimum of preparation. The resolution however, is capped to half the used wavelength. This can be a problem when very small structures are handled. Nevertheless, for the purpose of device characterization and defect identification, common microscopic techniques are sophisticated enough, as explained in Chapter 2.2.

For characterization methods the optical inspection is the most simple, most used and most informational method. The inspector checks for homogeneity of the surface and/ or the sample's interiors. While the former can be easily done with any microscope and visible light, the latter is bound to the transparency of certain materials to certain parts of the light spectrum.

As explained in Chapter 2.2.1, most (compound) semiconductors are at least partially transparent to IR light. This makes it the region of interest for optical inspection. Due to the fact that most defects in a crystal's structure are of μm scale, the minimal resolvable structure of (near-) IR light is smaller than the average size of a defect structure. These structures that cause disturbances of the crystal lattice homogeneity for CZT can be categorized by known crystal defects, such as those listed in Table 8.1.

In parts of these defects excess of Te accumulates, which appears due to dominant evaporation of Cd during CZT growth. As it was shown in Chapter 2.2.2, tellurium is generally opaque to IR light for $\lambda < 4\,\mu$m, while Cd and Zn are rather transparent[1]. For this reason, these types of defects are promising candidates for detector quality evaluation by means of IR-optics.

Te-filled defects (of various sizes and shapes) are associated in the literature with crystal structure disturbance, carrier trapping and decrease of resistivity. Although the resistivity decreases because of the missing Cd and not because of the Te condensed in the vacancies. Nevertheless, since the Te condensate (inclusions) can be directly detected, the decrease of resistivity is loosely explained with these inclusions.

[1] In the region of 875 nm to 2750 nm used for this work.

Another group of defects represents boundaries between single-crystal grains or regions with different lattice properties. These can be decorated with Te-precipitates that will show up in large contrast on an IR image.
All these defects are unwanted for CZT detectors. In the case of productive processes, the areas of an ingot that do not show high density of Te inclusions or grain boundaries are chosen to cut the detector blanks from it.

Panorama Observation - IRP

Before a crystal is scanned in detail a preliminary investigation of the whole sample is done to determine if it is worth testing the sample any further.
At the present stage of the test system this is done in a table magnifier with adjustable magnification (0.75-5 x) and a simple IR-LED (950 nm) as a light source. In the second stage of research this test will be integrated into the same system with the other test methods of this chapter, as it is schematized in Figure 8.11, Appendix B.
The crystal is investigated in transmission. All major damages and defects are identified and recorded according to Table 8.1. Furthermore, an image with both IR and VIS light is recorded to determine which of the defects are internal and which are results of surface damages (Figure 3.2). This information is of importance, because surface damages can be partially removed by further processing the sample.
This method is also of great importance for the industrial production process of a de-

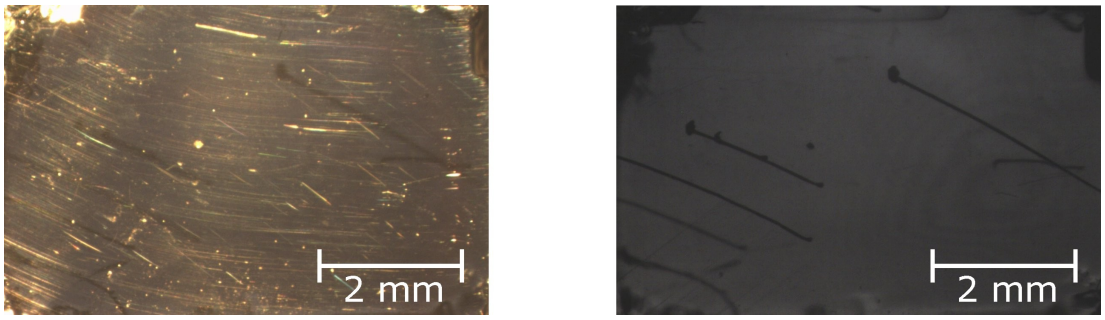

Figure 3.2: Panorama IR/ VIS image of a CZT crystal with prolonged gas void defects. - The defects are interior which is revealed by the golden scratches in the image on the left.

tector, since in this stage the areas of a grown ingot that contain major crystallographic

defects are separated from areas without. A schematic drawing of this test is provided in Figure 3.3.

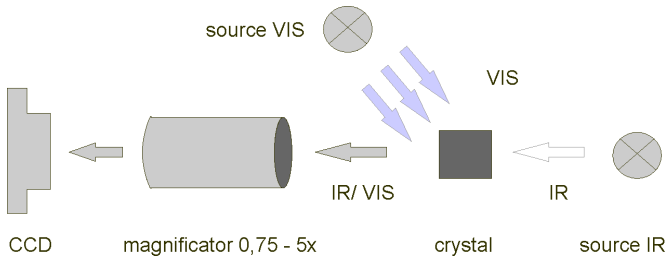

Figure 3.3: Schematic of an IRP scan - The crystal sample is illuminated either with IR-light in transmission, or with both IR and VIS. The image is recorded by a CCD-camera without IR filter; the second light source emits in reflection.

Infrared Microscope Imaging - IRM

After a sample has passed the panorama test, it has to be scanned for microscopic inclusions. Their size is much smaller than macroscopic defects such as cracks and voids of mm size. These microscopic defects affect the detector's performance by their numbers. Microscopic defects (usually Te inclusions) disturb an induced signal by trapping passing charge carriers and decrease the material's resistivity. For that reason, the reduction of the number of inclusions is one of the main efforts of CT/ CZT growth research. This is why it is of great importance to know about the number, size and position of these inclusions within a given sample.

For commercially available crystals this information is only done on a scale of panorama[1] observation. Such a IRP image reveals only the largest inclusions on a 2-dimensional distribution. However, a 3-dimensional (3D) scan provides insight about the processes occurring during the growth of an ingot and helps to improve the procedure as it is done by (*Ezzat et al.*, [15]). Based on this research, the method has been adopted and improved to be included here. The scanning principle is schematically visualized in Figure 3.4.

The crystal is mounted into the test system for the combined methods, between the rubber electrodes (Figure 8.5 Appendix B, in this test used for protection). Hereafter it is moved in three dimensions within the focus of a long working distance microscope objective. If no treatment of passivation has been performed on the crystal, it can now

[1] One image covers the whole crystal, as in Figure 8.3.

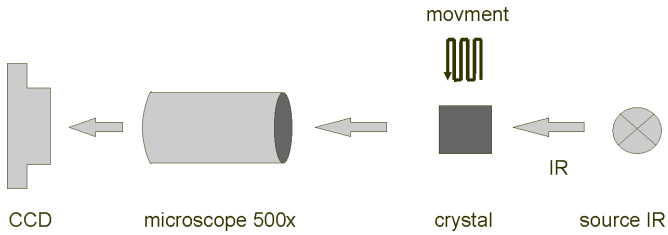

Figure 3.4: Drawing of the IRM scan principle. - The crystal sample is moved in 3 directions within the focus of a microscope, while being illuminated in transmission with an IR-light source. The image is recorded by a conventional CCD-camera without IR filter.

be scanned in IR light according to a predefined script. Here the white light source of the IR-Spectrometer (needed for the IRS test, following section) will be used as a light source, for which the crystal itself will act as a low band filter by blocking wavelengths below it's IR transparency (starting $\approx 875\,\mathrm{nm}$) and the silicon of the CCD chip as a high band filter. Most CCDs (as the one used) have a VIS detection efficiency of less then $1\,\%$ for wavelengths $\geq 1\,\mu\mathrm{m}$.

Due to the impossibility of realigning a sample exactly at the same position as the previous one and the usually differing size of the samples, a movement script has to be written for each crystal individually. This is done by finding the movement distance of a sample (in μm) the stage needs to travel from one side of the crystal to the other. This is relatively simple for the length and height of the sample (x, z-axes), whereas the displacement in depth (y-axis) has to be accounted for. This displacement movement is more challenging since the surface can have little hills and valleys. Another important issue is that the actual movement (of the focus) within the crystal in y-direction is compressed by the factor of the material's refractive index ($n_{CZT}(\omega) = 2.76$ [1]). Which e.g reduces the physical length of a typical crystal from $5.0\,\mathrm{mm}$ to an optical length of $1.81\,\mathrm{mm}$ [2]. After finding the crystal's dimensions as it is 'seen' by the camera the movement steps are defined. This is basically the number of scan points per axis, minus some surface space ($\approx 400\,\mu\mathrm{m}$), because the most serious defects are located close to the surface.

The used stage (Steinmeyer MP63-25-DC-R) has a higher accuracy for a continuing small movement in one direction than going back and forth on long distances [30]. This is why a script should be written to prefer small steps in one direction. Starting from

[1] $n_{CT}(\omega) = 2.79$
[2] CT $= 1.79\,\mathrm{mm}$

one corner of a sample the movement follows an S-shaped curve on the x/z plane, returning to the starting position (for control purposes) and is then continuing to the next plane in depth by moving into the y-direction. Such a movement is visualized in Figure 3.5.

For the first plane the focal point is set to a distance, in front of the crystal, where no

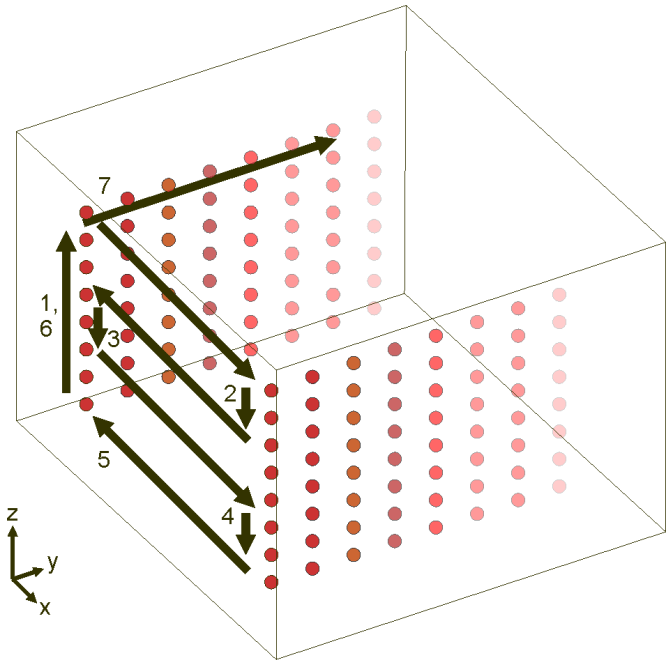

Figure 3.5: Illustration of scan movement during a IRM/ IRS test. - The scan is done in planes, facing the objective. For better oversight the number of columns (red dots on the x-axis) has been reduced to the first and last ones only.

surface structures of the crystal are recognizable ($\approx 300\,\mu$m). The images, very blurred gray distributions, will be used as the background data for the calculations done later in the analysis.

Infrared Spectroscopy - IRS

As demonstrated in Chapter 2.2.2, Te is opaque to near IR light, due to its high reflectivity. This results in the observed and theoretical predicted ([11], [12], [15]) transmission intensity of $\approx 66\,\%$ for CZT. Inspired by the way the IRM method is done, the same

procedure can be applied to infrared spectra. By taking IR spectra from different positions of the crystal (e.g. the same positions at which IRM images were taken) and comparing these spectra to each other, one can produce a map of the relative Te distribution within that crystal[1]. The more uniform that map is, the more uniform the crystal has been grown, which presumes the better detector energy resolution due to more effective charge collection after an incidental ionizing event. The charge collection efficiency depends on the mobility-lifetime product of the charge carriers and on the uniformity of the applied electric field, and is both directly and indirectly a function of the Te distribution within the crystal. A visualization of this distribution is therefore important to better understand the material.
A slight difference in the amount of Te will already lead to a difference in IR transmission in that area, which the highly sensitive spectrometer will detect. E.g. 66 % transmission intensity has a specific value for the spectrometer, anything different from that level provides information about more or less Te distributed in that area, compared to the previous one. Hence more or less trapping centres or electric field distortion regions in that area.
Furthermore, these spectra can be acquired in areas where the normal IR image does not reveal any inclusions, which by the IRM method is indicated as good crystal structure for that area.
An interesting aspect of the new IRS test method is that exactly the same test set up can be used as for the IRM method. Only the recording device needs to be changed from CCD-camera to the spectrometer detector. This makes the integration of both methods into each other very simple. A schematic drawing of the test principle is provided by Figure 3.6 below. The used IR-Spectrometer is a *Thermo Nicolet 6700*, model 2010.

3.1.3 γ - Spectroscopy

To compare and judge results from earlier test methods, an 'in vivo' test has to be performed to a detector crystal. This is done by recording the electrical response of a detector crystal within the flux of a radioactive source, such as Cs-137 or Am-241. If

[1] Assuming Te is the major reason for changes in transmission and therefore measured intensity.

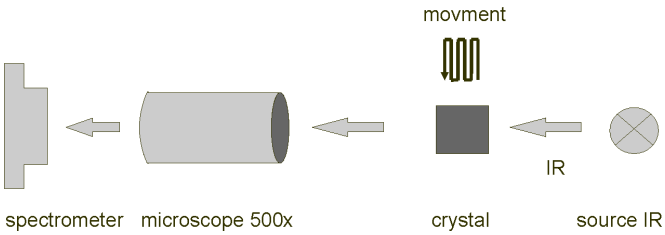

Figure 3.6: Drawing of the IRS scan principle. - The crystal sample is moved in 3 directions within the focus of a microscope. While being illuminated in transmission with an IR-light source. The spectrum is recorded by IR-Spectrometer. Note the similar setup to the IRM method, Figure 3.4.

the crystal does not possess electrodes, then the missing steps of production[1] will be performed.

Afterwards the crystal is placed in a γ-Spectrometer which consists of a spectrometer holder, a charge sensitive and linear amplifier and a multi-channel analyzer (Figure 3.8). The captured signal is displayed on an oscilloscope and recorded to a file. The performance of the crystal is judged by its capability to resolve points of interest within a given spectra. Such as the 662 keV γ-peak of Cs-137 and the 59.5 keV γ-peak of Am-241, as it is shown in Figure 2.11. The better the ratio of peak to full width half maximum (FWHM), the better the crystal's performance will be.

The spectrometer holder (casket) has been designed to temporarily apply a high volt-

Figure 3.7: γ-Spectrometer. - The most important parts of the spectrometer are the holder (*right*) and the preamplifier *left*.

age to a crystal. This casket can be seen in Figure 3.9. The most important task of the holder is to reduce the noise. This is why the device itself cannot be of diamagnetic

[1] Which in most cases are chemical application of gold electrodes as well as surface and optical passivation by several different etching processes.

materials such as aluminium alone. It needs to be a paramagnetic material to shield both electric and magnetic fields. Additionally, only highly conductive (steel, brass) and isolating (Teflon) materials can be used. Also, all contacts are soldered (the reason for brass) and screwed to ensure that a low noise connection has been made. Then the crystal is placed between the electrodes and a source (Cs-137, Am-241) is placed on top, facing downwards.

The readout circuit is schematized in Figure 3.8. The casket is connected to a charge sensitive preamplifier which itself is connected to a linear amplifier. The output signal from the linear amplifier is displayed on an oscilloscope and forwarded to a MCA which is records the spectrum. Furthermore, a pulse-generator is connected to the scope and the preamplifier to provide a calibration signal. The second most important device

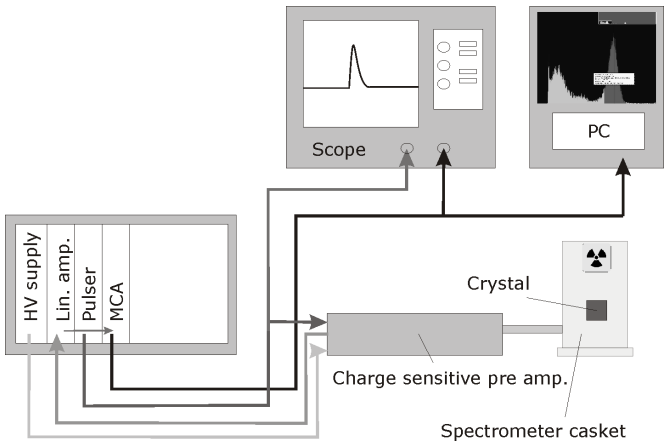

Figure 3.8: A schematic drawing of the readout circuit of the γ-Spectrometer. - The radioactive source is placed inside the casket with the detector. The most important devices - the casket and the preamplifier - should be connected by a short cable to further reduce noise further.

in that chain is the preamplifier to capture the electrical signal from the crystal. Due to the high resistivity of CT/ CZT and the small size[1] of a normal crystal, this signal is in the order of μV. For this reason, the amplifiers need to have a sufficient amplification factor, but still be suitable for small input capacitances. The AmpTek A250CF [34] and the Caberra Modell 2004 [33], second with an amplification of 45 mV/ MeV for silicon, are suitable devices. With the Canberra device a Cs-137 signal (0.662 MeV,

[1] Usually cubes with a side length of 5 ... 10 mm.

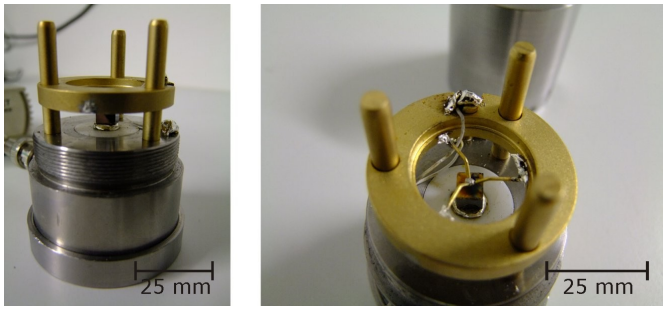

Figure 3.9: Holder (casket) of the γ-Spectrometer. - The device is made of mainly steel and Teflon to ensure highest noise shielding.

γ-emission) is expected to produce an amplitude of 29.8 mV on the output channel[1]. With possible noise levels of several mV, the highest standards of shielding are needed to achieve reasonable S/N-ratios of approximately 15/ 1. Additionally, these devices are optimized for Si-detectors. CT/ CZT detectors with a larger bandgap than Si are expected to produce signal amplitudes of up to 25 % less on the preamplifier's output channel.

3.2 Test Methods of the Second Stage

In this section, the tests for crystal characterization that are to be included in the second stage of the research are briefly outlined. An schematic presentation of the integration of all methods into one test system is provided in Appendix B (page 77).

3.2.1 Electrical Field Analysis via Pockel's Effect

The Pockel's effect is the electrically induced optical effect which will change the polarization of passing light as a function of the applied voltage.
Crystals that lack inversions symmetry (such as CD/ CZT) possess this effect. For this test, linear polarized light is used to illuminate a sample. After passing the sample the light is totally eliminated with a second crossed polarizator (= analyzer). If the crystal

[1]The AmpTek A250CF has an amplification of 176 mV/ MeV for Si. The Cs-137 γ-signal will have an amplitude of 118.5 mV on the output channel. Respectively 10.65 mV for the most prominent γ-emission of Am-241 source at 59.5 keV. While the Canberra device is expected to produce 2.67 mV for the Am-signal.

has a (high-) voltage applied, the electro-optical effect develops and will change the light's polarization slightly as a linear response to the applied field. Due to this change, the light can not be fully cancelled at the analyzer anymore. A camera after the analyzer can capture the remaining intensity which is the squared function of the electric field. Non-linearities in that function are therefore directly related to non-linearities of the electric field and so to inferior crystal quality. For imaging and spectroscopic applications, a crystal's linear signal response on a radiation signal is a crucial point. More information can be found in [17] for example. Due to the importance of this information for understanding the growth process, this method is prioritized to be included in the second stage of this research (see Figure 8.14, Appendix B).

3.2.2 Internal Stress-Test

Because the growth process of CT/ CZT still contains many unknown processes, the crystalline quality compared to grown silicon is usually inferior. Common problems are structural stresses that result from the growth method (e.g. material freezing too fast). These stresses are manifested in misaligned crystal layers and planes, which lead to centres of charge trapping and disparities in the electric filed. As a result, the detector's spectroscopic and physical performance suffers. These stresses can be visualized, due to the effect of birefringence, by taking crossed-polarized IRP images of the crystal without bias voltage [18]. Due to the origin of these stresses − defects in the crystal structure − the light will be slightly polarized when passing the crystal. Therefore, an image that should be black due to the crossed polarizers will show areas of light. An electric field will most likely be non-linear in these areas. The absence of this is an essential aspect for certain applications such as imaging. To know if and where these stresses are present, will provide the information needed for further treatment (possible cut out/ off), and will help to further understand the growth process. An integration of this process into the existing test system is presented in Figure 8.11 (Appendix B).

3.2.3 Contactless Resistivity Measurement

CT/ CZT crystals are very fragile (2.9 on Mohs-scale of hardness), and the use of metal needles always damages the surface of a sample. This is one of the reasons for degradation of a detector's performance. Furthermore, the best results from standard test methods (e.g. 2/ 4-probe method) are only received if contact electrodes are applied

to the sample. This implicates the complete processing (into a radiation detector) of the crystal, a costly and lengthy process. For this reason; the accurate measurement of resistivity in an early process stage is of great value for research and industry.
There are several methods of contactless resistivity measurements as proposed by [19] for example. These methods are based on measuring the dielectric response of a crystal on an alternating electric field. Hence, by measuring a capacitance and using the crystal as a dielectric material, the resistivity can be calculated. This process can be easily integrated into the optical characterization system as it is schematized in Figure 8.10 (Appendix B).

Synopsis

In this chapter the characterization methods for CT/ CZT were presented and described. In the case of the first stage methods, a detailed functionality and realization has been provided. To acquire data of the whole bulk material of a crystal, the method presented by *Ezzat et al.* [15] had been modified and automated to scan a sample in three dimensions. Additionally this idea was further adapted to be used with (part of) the infrared spectrum, and the IRS test had been developed as a new method for characterization.
The second part of this chapter briefly covered the characterization methods that are to be included in the second stage of research, as well as their integration into one combined test system (Figure 8.10 - 8.17).

This page is intentionally left blank

4

Experimental Data

The introduction stated that the data obtained by each method is collected within this chapter. The reason for this is that it is more illustrative to compare the data of each method to one another, since this comparison is the main goal of this work. Furthermore, certain aspects of the data that are of interest for the following interpretation are pointed out here.
The order of topics addressed here is the same as in the previous chapter: first a presentation of what the data of the resistivity test will look like, then the IRP, IRM and IRS methods. Finally, spectra from the γ-tests are presented. Additionally, when it is of use, examples of good and bad data sets are presented. During the process of data acquisition the environmental conditions (temperature, pressure, humidity) were monitored. Temperature and humidity were kept within a variation of 5 %.

4.1 Resistivity Measurements

The data for the resistivity was acquired as described in Chapter 3.1.1. Since the equation (2.3) takes the physical sizes of a crystal into account, these values have to be recorded as well. This is done with a standard caliper with Teflon protectors applied to it's outside jars. This has been done to protect the crystals from physical damage. Additionally, the resistivity is averaged for values obtained from the complete voltage sweep (0 - max - 0) V and not only recorded for the operation voltage of the final detector. An example of such a sweep is demonstrated in Figure 4.1.
The averaged error $\Delta\bar{\rho}$ of this method is mainly determined by the accumulated error of

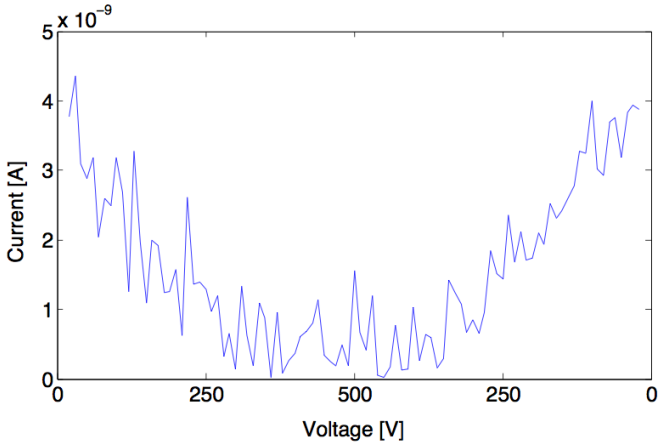

Figure 4.1: I-V curve obtained by the resistivity measurement with the 2-probe station. - The voltage sweep is performed from 0 V to maximum (500 V) and back to 0 V to ensure that the nonlinear region has not been entered nor the crystal damaged.

the claiper (0.05 mm) measurement, while the variations of the power supply ($< 10^{-5}$ V) and picoammeter ($0.3\,\% + 400$ fA) can be neglected. The error of the caliper on the other side is tripled due to the measurement of all dimensions of the sample.

The maximum voltage is determined by the thickness of the sample[1]. 100 V per mm is a common step size for CZT. In addition to the average resistivity $\bar{\rho}$, the maximum resistivity ρ_{max} for a sample is listed in Table 4.1 [2] as well to support conclusions drawn in the next chapter.

For the batch of quality samples, values of resistivity are supplied by the producer ISC [35]. These are used to verify that the chosen test method will provide consistent data. For this reason Table 4.1 contains two values of $\bar{\rho}$ for the *ISCqual_sampA*. The one calculated from the supplier's value is marked with an *asterisk*. The order of magnitude of the producer's resistivity value differs [3] only slightly from the measured one. This has been repeated for all quality samples with similar results. Therefore, the data obtained with the 2-probe method is considered to be correct.

A complete table of resistivities for all samples covered in this work can be found in the Appendix B 8.2.

[1] Since the leakage current is a function of the resistivity which itself is a function of the thickness.

[2] Note that the resistivity in this work is given in units of definition [$\Omega\,\mathbf{m}$], instead of the unit commonly used in semiconductor industry [$\Omega\,\mathbf{cm}$].

[3] $\mathrm{R}_{measured} = 6.06 \cdot 10^{11}\,\Omega$, $\mathrm{R}_{ISC} = 1.3 \cdot 10^{11}\,\Omega$

Table 4.1: Sample resistivity for each tested group of crystals - Ordered by process steps. The maximum resistivity is ρ_{max} and the error is $\Delta\bar{\rho}$.

Group	**sample name**	$\bar{\rho}$ **in** $[\Omega\,\mathrm{m}]$	$\bar{\rho}_{max}$ **in** $[\Omega\,\mathrm{m}]$	$\Delta\bar{\rho}$ **in** $[\Omega\,\mathrm{m}]$
Polishing	*ISCpolish_samp2*	$1.10 \cdot 10^{10}$	$4.37 \cdot 10^{11}$	$7.75 \cdot 10^{8}$
Etching I	*ISCetch1_samp2*	$3.86 \cdot 10^{9}$	$7.91 \cdot 10^{10}$	$3.45 \cdot 10^{8}$
Etching II	*ISCetch2_samp3*	$5.06 \cdot 10^{9}$	$8.77 \cdot 10^{10}$	$4.31 \cdot 10^{8}$
Doping	*ISCdope_samp2*	$4.86 \cdot 10^{9}$	$7.91 \cdot 10^{10}$	$3.18 \cdot 10^{8}$
Quality	*ISCqual_sampA∗*	$0.97 \cdot 10^{9}$	-	$6.07 \cdot 10^{7}$
Quality	*ISCqual_sampA*	$4.51 \cdot 10^{9}$	$4.23 \cdot 10^{9}$	$2.95 \cdot 10^{8}$
Resistivity	*ISCres2_samp3*	$7.25 \cdot 10^{9}$	$1.42 \cdot 10^{11}$	$4.65 \cdot 10^{8}$
AcroTec	*Acro8.5*	$5.15 \cdot 10^{10}$	$4.70 \cdot 10^{11}$	$8.66 \cdot 10^{9}$

4.2 Infrared Panorama Observation - IRP

The defects by the transmission investigation recorded are usually scratches on the surface, cracks, grain boundaries and large inclusions. These identify themselves (in named order) with long black lines, crushed like areas, thin dotted long lines (therefore appearing gray) and black round areas, as can be seen in Figure 4.2 and Figure 8.3, Appendix B. The found defects are written into a database so that later access to this crystal's specific information is possible. Samples that contain major defects (number 6 - 8 in Table 8.1) are taken out of the testing process.

In this test a sample will pass if it does not contain major crystallographic defects such as prolonged (gas) voids, grain boundaries and cracks. Minor defects such as surface scratches and small inclusions are acceptable if the sample's resistivity is high enough ($> 10^{9...10}\,\Omega\,m$). In this case, the sample can still be produced into a working detector for plain detecting purposes (no imaging or spectroscopic applications).

To reduce possible misidentifications of defects, the influence of the plastic base tray as the background has to be taken into account. This can be accomplished by taking an IR image of the empty tray. The background image is processed and subtracted from the IRP image of the CZT sample. By this process, defects such as scratches on the plastic tray appear white in the processed IRP image. Additionally, inhomogeneities of the base plate (dark cloudy areas in Figure 4.2) are emphasized as well. Finally, the crystal is moved on the base plate several times and the images taken are compared to each other. By this procedure, stationary defects (e.g. the dark cloudy areas) are identified.

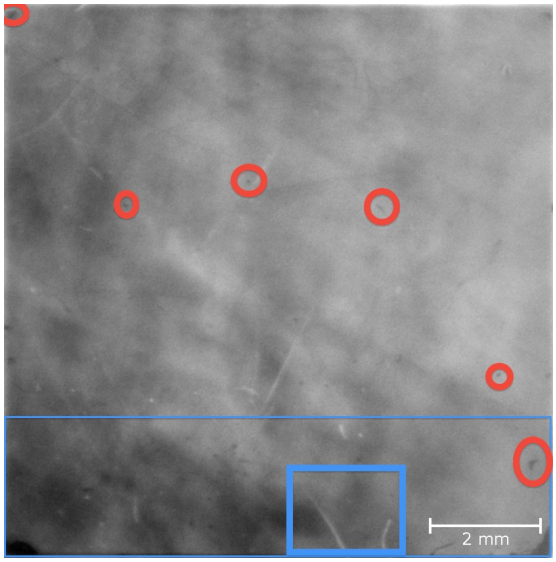

Figure 4.2: IRP image of a clean sample, almost no crystal defects can be identified. - Orange circles mark some the identified defects, while the blue boxes mark background induced flaws such as long white lines and black cloudy areas. Image had been processed to better visualize the defects, due to this process the background induced cloudy area appears worse than on the original image.

4.3 Infrared Mircoscope Scan - IRM

After a crystal has passed the IRP test it is mounted into the optical testing system and scanned with a script according to 3.1.2. After all the data has been recorded, it is processed and analysed using Matlab. This processing basically includes enhancing the image, subtracting the background, finding and counting edges. In the next step the found number (of inclusions) of that image is put in a 3D-map, at the position of the originally recorded image. This way a comparable view of the found defects to the actual position within the crystal is made. Such is presented in Figure 4.3 and a processed image with a successfully found inclusion in Figure 4.4. The information of found inclusions and the corresponding positions of the record are put into the database as well. The number of falsely counted (too many/ too few) inclusions is used for an error analysis and covered in the next chapter, section 5.3.

Such maps as of Figure 4.3 will provide only a very subjective view of the inclusions found inside a crystal, because these figures are only 2D projections of the 3D distribution. In most cases such a map contains hundreds of coloured bubbles which partially

superimpose each other, that these maps will always look very full[1]. A better understanding is achieved by viewing the interactive figure in MatLab. Here the viewing angle can easily be changed and the positions of the inclusions better realized.
These position maps of the detected inclusions within a crystal, as well as the inclusion numbers at certain position, provide highly useful information for the research of the growth process of CT/ CZT. For a comparison of characterization methods, however the overall number is of greater value.

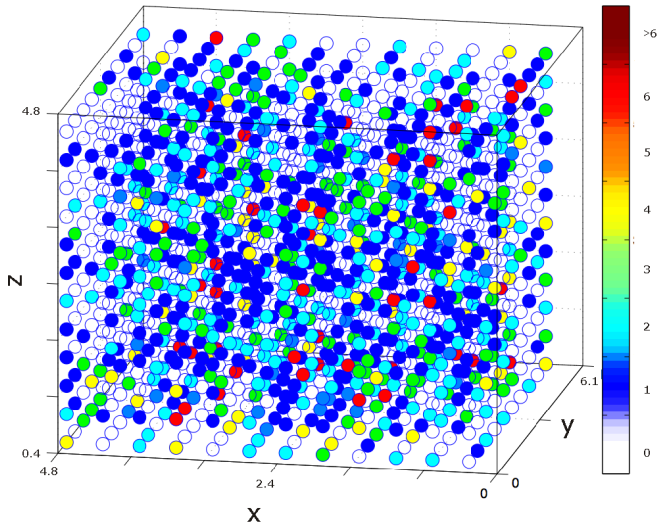

Figure 4.3: 3D map of the spatial distribution of Te inclusions in a crystal. - The color code refers to the number of inclusion found in that location. Clear = 0, or blue = 1 is better than dark red ≥ 6. The total number of inclusions is 1234. The axes *x, y, z* are in mm.

4.4 Infrared Spectroscopic Scan - IRS

Since a movement script of the positions for each scan-point is already available, the crystal is also scanned for infrared spectra at the same time. Therefore, not only a detailed microscopic scan is available, but also a spectrum of the transmission intensity for each of these coordinates. Due to the specific transmission of the raw materials (Cd, Zn, Te) and absorptions edges of the other used materials (e.g. glass, filters), the chosen spectral interval ranges from 875 - 2750 nm (11428 - 3636 cm^{-1}). In this interval

[1]Unless the crystal's physical dimensions demand a limitation to the scan in one direction, as for the AcroTec samples, Figure 8.6 left side.

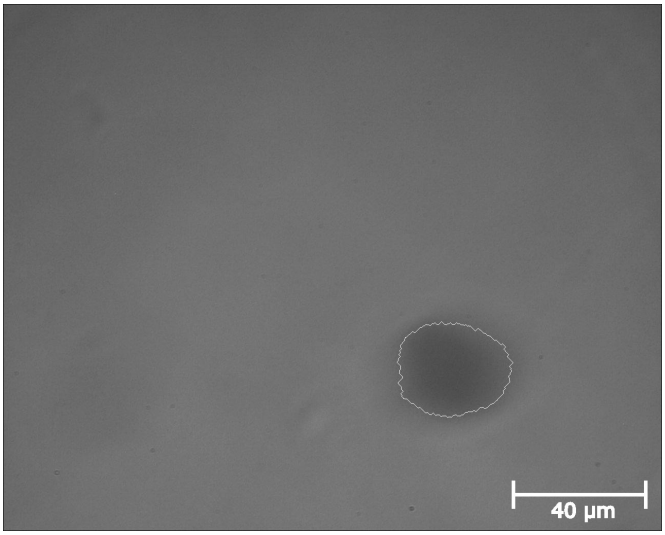

Figure 4.4: Processed image after the IRM inclusions detection process. - The found Te (dark area) inclusions are marked with white edges and counted. The picture is not enhanced.

the transmission intensities are 33 % (Cd) and 41 % (Zn) and 0 % (Te), as it is derived in 2.2.2. Other optical components are chosen with a transmission intensity[1] as high as possible. Although this is not completely achievable, all transmission reductions outside the crystal can be accounted for towards the background, because these values will not change during a measurement. This way all changes in intensity can be accounted for towards the Te absorption within the crystal.

These spectra are processed and analysed with Matlab as well, which follows in principle the same pattern as for the IRM analysis: enhancing by subtraction of the background and averaging the values. Each of these averaged values are then put into a 3D-map at the coordinates of the obtained spectra. Again an illustrative representation of the actual crystal and in this case the submicron Te distribution is generated. Such an obtained 3D-map is presented in Figure 4.5. The colourmap on the right of this figure is the relative dynamic transmission range of that crystal and is given in arbitrary numbers. A larger scale indicates a larger overall variance of transmission within the tested sample. Therefore, a smaller dynamic range indicates better crystallographic

[1] Quartz glass shows transparency until about 3.5 μm, but due to water inclusion the transmissions signal get distorted at 2.75 μm. The used polarizers transmission is $\approx$ 75 % [31] and $\approx$ 62 % for the beam splitter [32].

homogeneity.

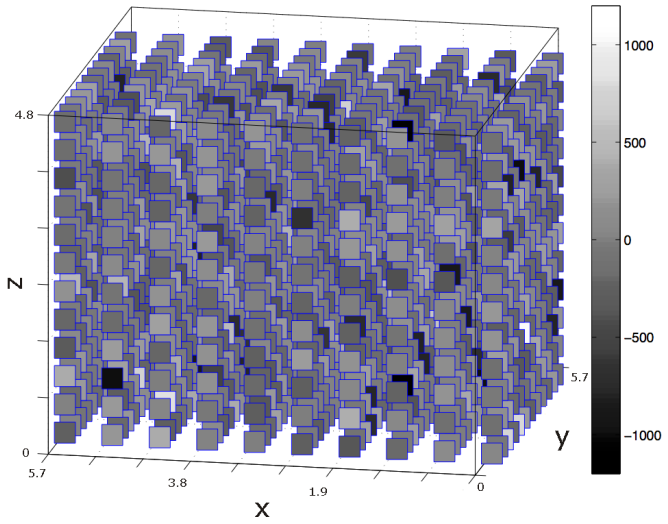

Figure 4.5: 3D relative transmission map of a crystal. - The color of the tiles refers to the relative intensity change in transmission of that location. The more uniformly around level 0 the distribution is spread, the better the crystals homogeneity. The axes *x, y, z* are in mm. Note: for better clarity, the view has been turned by 90° to the right, compared to Figure 4.3.

4.5 γ - Spectroscopy

The recorded γ-spectrum of a crystal can be processed in the program provided with the MCA. The energy values of the peaks, FWHM, as well as the spectra itself, can be copied to a database directly from the program, and no further processing needs to be done. Within the scope of this work, background and source spectra were recorded, peaks and FWHM found and compared to reference spectra for CZT. A crystal's performance is better if a peak is recorded at a higher energy (eV [1]) with smaller FWHM, while the gain, shaping time and bias voltage are kept on the same levels as for another crystal. All after subtracting a source spectra from its background for that sample. Before the spectrum is recorded, special attention has to be paid to sources of noise that cause signal broadening. Test spectra without bias voltage and radioactive source help to identify the causes of noise. These are usually induced by the leakage current of the crystal, interfering electromagnetic radiation[2] and the readout electronics itself.

[1] recorded in channels by the MCA
[2] cell phones, power grid, fluorescent lights

An example of a good (*left*) and a bad (*right*) spectra are presented in Figure 4.6. The background noise of the good example is due to the used low gain of the linear amplifier (10 ... 300) and effective signal filtering of the preamplifier, which is very small compared to the bad sample on the right.

Due to the strong influence of the crystal's processing, the used electrodes and the read out system as well as its tuning to the crystal's capacitance, the data of this test is subject to too many variables for a reasonable comparison. For this reason, only a qualitative assessment will be done. Nevertheless, this qualitative analysis is sufficient enough for the comparative aim of this work.

(4.6)

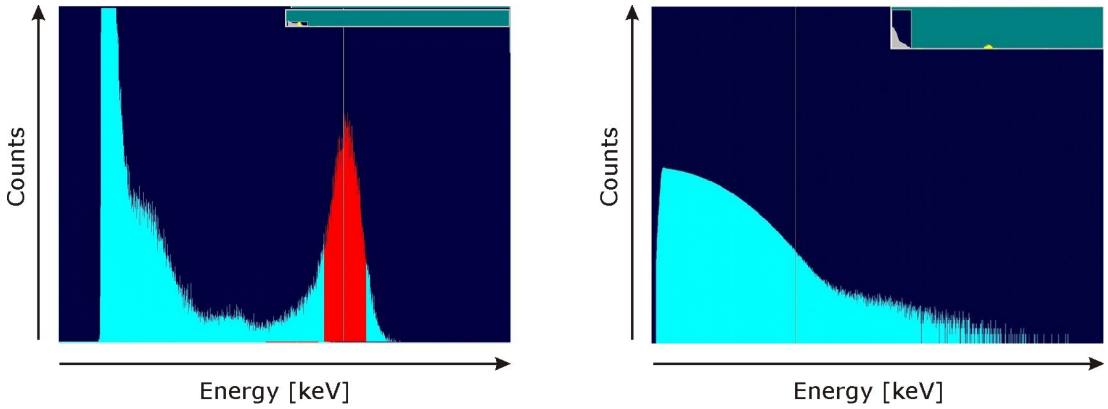

Figure 4.6: Comparison of Am-241 spectra of a good and bad crystal. - The one on the *left* shows a clear peak for the 59.5 keV γ-emission while the one on the *right* is dominated only by noise.

Synopsis

Within this chapter, the data obtained from every test method and its consistency has been presented, and special features have been pointed out. These features, such as the total number of inclusion or the dynamic range, are especially investigated in the next chapter and put into context with established characterization attributes such as the resistivity.

5

Comparative Analysis of Each Method

All tests were performed in the order of resistivity, IRP, IRM/ IRS and the γ-test. The γ-test was performed last not to bias expectations and the treatment of the samples during the other tests. By this meaning, the resistivity test should have been done second to the last, also to avoid bias. The reason for not doing so is that the resistivity information was needed to increase the data diversity (by choosing the best and worse sample of each batch) and therefore the accuracy of possible performance predictions. During the daily business of characterizing CT/ CZT crystals, the order will be IRP, IRM/ IRS, resistivity, γ[1] - test.

Since all crystals originate from different production batches (different parts of an ingot, different ingots) comparisons are very difficult. Because it is not possible to produce similar ingots as it is for Si for example, a comparison of the characterization data from CT/ CZT is an ambitious task. It was found in Chapter 2.3.1 that a radiation detector will perform better with higher resistivity. For this reason, the data from all characterization methods will be compared to the resistivity of a crystal and to the resistivity of all other tested samples. Therefore, Table 8.2 is the basis for comparison in this work.

This is a reasonable approach because all tested samples have a fact in common: the

[1] One of the objectives of this work is to predict a samples resistivity and γ-performance from the data obtained with the IRM/IRS methods.

amount of Zn as a matrix element [1]. Furthermore, the final evaluation aspect is the performance of the detection of a γ-signal which, as pointed out earlier, is mainly determined by the resistivity of the material.

5.1 Resistivity Measurement

In Table 8.2 a rank has been found for all tested crystals. This rank is the strict order of increasing resistivity $\bar{\rho}$. A higher rank number will be interpreted as a crystal of better quality. This rank number will be used for classification in other tests.
From this Table 8.2 it is confirmed that the surface treatment increases the resistivity, as can be seen for example, by the numbers of the etching processes. The explanation of this is the reduction of the damaged surface layer, where charge trapping, contact barrier effects and accumulation of impurities from the environment into a number of micro cracks occur. These pollutions have less impact on the charge carrier movement and therefore on the signal after the treatment, which increases the samples resistivity.

An interesting aspect of the resistivities calculated in Table 8.2 is that the values of the crystals ranked 18 - 22 are larger than the theoretical maximum of $(5 \cdot 10^9\,\Omega\,m)$ for $Cd_{0.9}Zn_{0.1}Te$, which is determined by the band gap. This obvious contradiction is intensively covered by Bolotnikov [21] and explained with an interfacial layer of several nm thickness between the bulk material and the electrode [2]. This layer can reduce the current passing the bulk material by several magnitudes which leads to a lower value measured at the current meter, and hence to a higher resistivity than the band gap can allow. Because this effect is similarly present for all tested crystals, it will be considered as an offset (2 - 3 magnitudes) to the true resistivity of the material. This first stage of research concentrates on the optical characterization only, and the investigation of this effect will not be covered further in this work. Nevertheless, the consistency of the results obtained from the other characterization methods support the chosen procedure of treating these higher values as an offset.

[1] $Cd_{0.9}Zn_{0.1}Te$
[2] The electrode is one of the metallic needles in the case of the 2-probe method.

5.2 Infrared Panorama Observation - IRP

This test observes if a sample contains major crystallographic problems such as prolonged gas voids, gain boundaries or cracks (# 6, 7 and 8 in Table 8.1). This has not been the case for all, but for only one of the crystals. To study the influence of a major crystallographic defect on the performance of that crystal and possible influences on the data from other tests, this sample was not taken out of the testing chain. Although, on the daily productive routine this particular crystal would not be tested further.
The majority of defects found in this test are of low or medium significance as graded in Table 8.1. However, some of the samples did show small cracks on edges and corners (such as in Figure 5.1), but these are not significant, because these defects are not present in the inner bulk material of the crystal. This is due to the fact that all

Figure 5.1: Small defect (crack) identified with the IRP method. - The magnified part of an IRP image. *Right*: IR image reveals the internal defects such as cracks (black areas). *Left*: Image with VIS and IR light of the same part to verify that the defect is internal. The black crack is below the golden scratches of the surface.

samples used in this work had been tested by the suppliers ISC [35] and AcroTec [36] previously. Only samples showing no major defects were shipped.

The one sample (*ISCpolish_samp3*) with defects of major significance (# 6, Table 8.1) contains some prolonged gas voids (Figure 3.2). These are not aligned parallel to the electrodes, and the void's cross section is interfering with the travelling path of the charge carriers and function as traps. This significantly deteriorates the signal quality. Since this sample does not show other major defects it is assumed that the difference in $\bar{\rho}$ compared to the *ISCpolish_samp2* is mainly due to these voids.

Another interesting aspect is that this method reveals if a crystal had been processed enough to be evaluated by any other optical test. A plain piece cut from an ingot has a too high surfaces roughness that all light is scattered away (similar to diffuser plates for VIS), and the crystal stays opaque to IR-light. Plain cutting and grinding the crystal

from the ingot will not provide the needed optical flatness. Only the next process step - polishing - reveals the desired attribute as it can be seen in the Figure 8.4, Appendix B.

5.3 Infrared Microscope Scan - IRM

5.3.1 General Discussion

Though a 3D map of inclusions[1] (Figure 4.3) provides a visual overview of how many inclusions are in which part of the tested crystal, it does not reveal immediately much more information.
From the first observation, a statement about the 'cleanness' of the crystal can be made. Empty bubbles are better than filled ones, more dark blue bubbles are better than bubbles in other colors. An uniformly blue map is better than a colourful one, but worse than a map with empty bubbles.
Statistically, red bubbles (≥ 6 inclusions) are more present at the surface than in the bulk material, while bubbles with less inclusions ($0 \ldots 4$ - clear ... yellow) can be found all over a crystal. This is an expected result, since the surface usually contains damages (e.g. scratches from processing, handling) and therefore has many defects, which are represented by red bubbles in this method.

A comparison between individual crystals is of no use due to the missing production data. Because the influence of this data on the distribution within a inclusion map can not be estimated, it has to be assumed that each crystal originates from a different ingot and therefore was grown under different conditions. A comparison of the spot numbers would be of great interest for samples from one ingot (e.g. top, middle, bottom part; outer, inner radius) to see how defects are spread during the growth process. As well as how this number is determined by the temperature-, pressure- and growth speed-profiles, which can be influenced during the growth. The feedback (number and position of the found inclusions) will help to improve the process and increase the production yield.

[1] Inclusions and spots are used as synonyms in this work.

5.3.2 Error Analysis and Classification

The number of inclusions (e.g. 1234 for *ISCres2_samp1*) is a undercount. The algorithms that find and count inclusions on the IR-images are set to a threshold that finds most inclusions for the majority of samples tested. This leads to a lower count of inclusions than there actually are in the sample, as is illustrated by Figure 5.2. Not all spots are found on an image (orange circles in middle image) or spots are found where none are present (blue circles in the right image). For an error estimation and

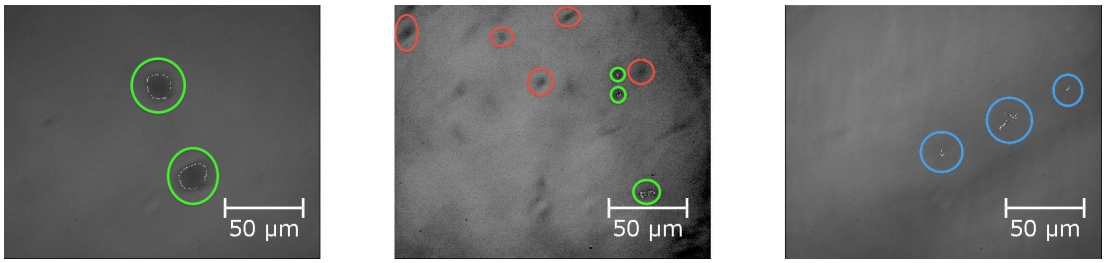

Figure 5.2: Errors of the IRM inclusions detection process. - *left*: exact counted inclusions - green circled, *middle*: undercount inclusions - orange circled (Note: image has been enhanced for better illustration), *right*: overcount inclusions - blue circled.

confirmation of how many miscounts occurred, a manual spot count of 50 IR-images was performed for 5 samples. Within these, a ratio of found to not found inclusions was determined and was averaged over all manually counted samples. Because detection threshold is the same for all tested samples, this ratio leads to an undercount of 54.8 %. This indicates that a better threshold should be found, but confirms that usually less inclusions are found than are actually in the sample, even with taking overcounts into account.

By drawing the individual miscount as an error of the found spots some interesting details are revealed, see (Figure 5.3). This graph suggests dividing the samples into three classes (low, medium, high quality) with individual spot detection thresholds to improve detection efficiency. The separation should be done by an attribute all crystals have in common: the resistivity.

Since the undercount is worst for the low resistive sample (here *ISC_res1_samp14*), best for high resistive (*AcroTec_8.5*) and relative constant for the remaining intermediate resistive samples a possible division would be the one presented in Table 5.1.

A certain number of undercounts is of use to cancel out possible overcounts such as the

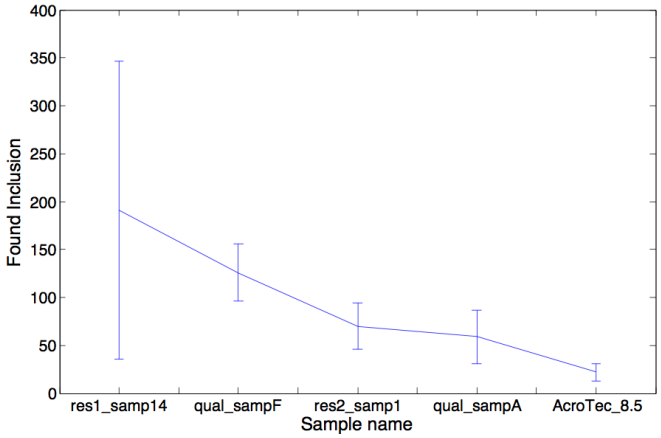

Figure 5.3: Comparison of the number of inclusions from several samples with not-found inclusions as error for each sample. - Ordered by decreasing number of found spots. Overcounted inclusions (detected not present) are subtracted from the error bar. The length of the error bar indicates that the chosen threshold will provide a relative undercount of 54.8 % for the majority of all tested samples. This ratio is better for higher quality crystals.

Table 5.1: Possible crystal classification - A classification for the quality of CZT crystals based on their resistivity.

$\bar{\rho}$ **in** $[\Omega\, m]$	**Class**
$\leq 10^7$	low quality
$10^8 \ldots 10^9$	medium quality
$\geq 10^{10}$	high quality

ones on the right in Figure 5.2. These overcounts occur more frequently with increasing crystal quality due to the lower spot to background contrast. The error received for the AcroTec sample is a possible option for a detection threshold. There the certainty of the correct number of found inclusions is 80 %.
Nevertheless, the absolute number of found inclusions is not of major importance. For this comparative work it is sufficient enough to work with a relative number of found inclusions per sample. This is why an adjustment to the detection threshold has not been done within the scope of this work, but has been postponed for further studies. To still be able to compare the number of found inclusions to other crystals, the number of found spots per scanned volume were scaled to $1\,\mathrm{mm}^3$.

5.3.3 Inclusions as a Function of Resistivity

Another interesting aspect of Figure 5.1 is that the number of inclusions decreases with increasing resistivity. In addition, to that the order of crystals in this figure is the same as it is for their rank in the Table 8.2, which indicates a connection between the number of inclusions and the resistivity of a sample. By plotting the found spots/ mm^3 as a function of resistivity for all crystals, this hypothesis is confirmed (Figure 5.4). For resistivities $< 2 \cdot 10^{10}\,\Omega\,m$ the number of inclusions is high (> 10) but stays relatively constant above that value, which leads to the conclusion that the number of Te inclusions are influencing the crystals quality only below a certain value (here $2 \cdot 10^{10}\,\Omega\,m$). Above this value the inclusions are scattered enough to be only of minor influence. The probability of charge trapping by a spot is low due to their spatial distribution. To visualize this, Figure 8.6, Appendix B compares the spatial distribution of found inclusions of a high resistive sample and a low one. The free path length for charge carriers is longer for the high resistive sample than for the low resistive one.
The fit in Figure 5.4 describes roughly the dependency of the number of inclusions on the resistivity. This information is of use for the research of CZT growth. Experienced groups can produce CZT of approximately aimed resistivity and simulation can be preformed better. Further statistics and research on this topic will allow to find better fit functions.

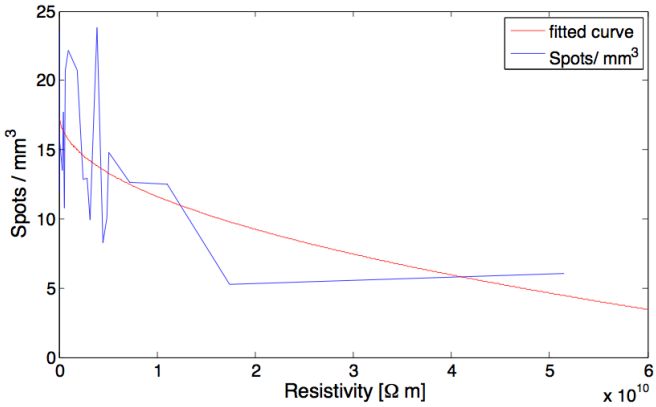

Figure 5.4: Number of detected inclusions per mm^3 as a function of the resistivity. - The tendency of the blue curve clearly indicates a connection between the number of inclusions and the resistivity of a sample. The fit is a power function.

5.4 Infrared Spectroscopy - IRS

5.4.1 General Discussion

Similarly to the spot analysis, the 3D map of IR transmission spectra does not immediately reveal much information. Nonetheless, the following conclusions can be drawn by carefully investigating a map such as the one in Figure 4.5 or Figure 8.7, Appendix B. The more uniform the color of all tiles is, the better the crystallinity and the charge collection efficiency of the investigated detector crystal is. Drastic changes, such as from gray (the crystals relative transmission mean) to black/ white tiles (maximum/ minimum relative transmission), indicate very high/ low IR transmission in that area. According to Chapter 2.2.2, this can be accounted for by more or less Te in that area. The dynamic range of the absorption is indicated by the colormap on the right hand side of the Figure 8.7 in arbitrary numbers. A larger range refers to larger differences in the transmission of that crystal.

By slightly changing the viewing angle (Figure 5.5), another interesting detail is revealed. The found extrema of absorption (black/ white tiles) are spread randomly over the crystal and are not accumulated near the surfaces as they are in the IRM test. This leads to the conclusion that the surface character is of minor influence for this method; a beneficial aspect for testing less processed samples. An explanation for this is that a IR-spectra of a tile is the average transmitted intensity of that volume. A scratch on the surface will reduce the volume of such that area only minimally, so an intensity

change is not as drastic as a higher density of Te in that volume. In comparison of

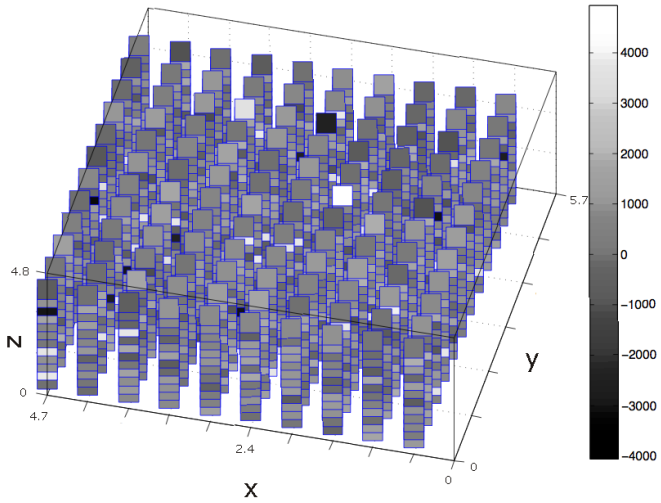

Figure 5.5: 3D transmission map of the same sample as in Figure 8.7, but under a different viewing angle. - The areas of high and low transmission (black/ white) are randomly spread. Surface damages that can be seen in the results of the IRM method are of no relevance for the IRS test. The axes *x, y, z* are in mm.

the transmission maps of a low and high resistive sample, one would expect that the map of a low quality sample (which corresponds to low resistivity) will contain more black/ white tiles than a high quality sample. However, Figure 5.6 does not support this assumption. The map of the high resistive sample has many black/ white tiles while the low quality sample's tiles are much more uniform. Furthermore, the dynamic range is 60 % larger for the high quality sample than for the more uniform map of the low resistive one.

5.4.2 Density Boundaries within a Crystal

When analysing the spectra maps, a particularity occurred in 41 % of the scanned samples [1]. This particularity, such as the one on the left side of Figure 5.7 below, partially shows the expected gray distribution (upper part of the image), but starts to be uniform from some point within the crystal (lower part, starting at layer 7). By plotting this uniform part only, it turns out that the dynamic range of the relative transmission in this area is much smaller than for the rest of the crystal (10000 vs. 800). This leads

[1] 22 crystals have been scanned.

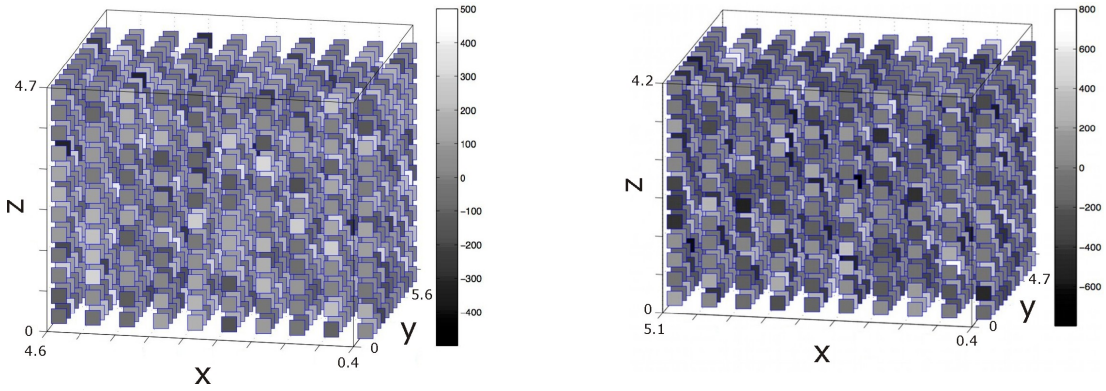

Figure 5.6: Transmission map of a low (*left*) and high (*right*) resistive sample. - The lower resistive sample shows a more uniform map than the higher one; the same applies for the dynamic range.

to a unified one gray-tone part on the spectra map of the whole crystal.

It can be concluded that this sample contains a boundary between two crystal blocks with a substantially different density of Te and therefore with a different IR transmission. A better representation of this effect is provided by Figure 5.8, which plots the

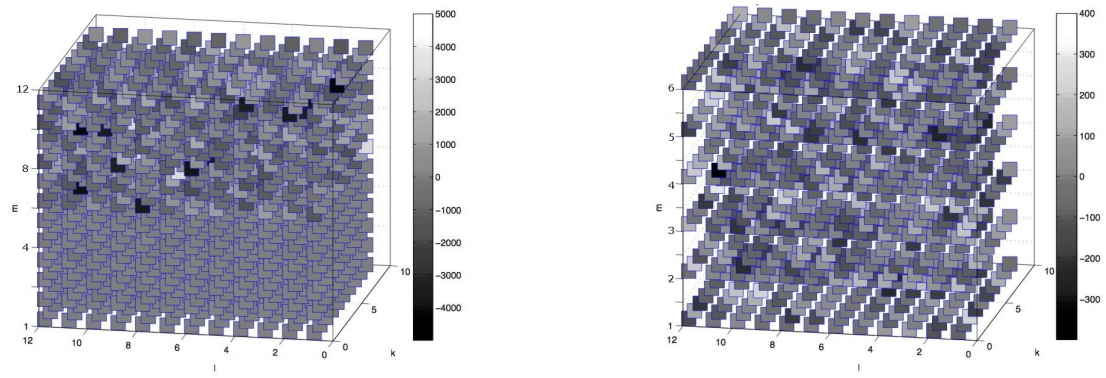

Figure 5.7: 3D transmission maps of a crystal with a Te density boundary (*left*) and a more detailed part-plot of the uniform area after the boundary (*right*). - The uniformity has a much smaller dynamic range which indicates better Te distribution in that region. Note: the axes are labelled in *k, l, m* which refer to the coordinate system used within the crystal. The scanned volume is $(4.3 \,\mathrm{x}\, 5.3 \,\mathrm{x}\, 4.2)$ mm in *x, y, z* direction.

transmission values of this sample as a function of the scanned plane. The course of the graph reveals that there is not only a sudden change in amplitude, but also that this amplitude varies strongly after plane 6 and that the overall transmission amplitude in this area is lower compared to the balanced first part. This lower transmission refers,

according to Chapter 2.2.2, to a higher Te concentration (but better distributed) in this area. By scanning the same sample with a higher scanning resolution (higher sam-

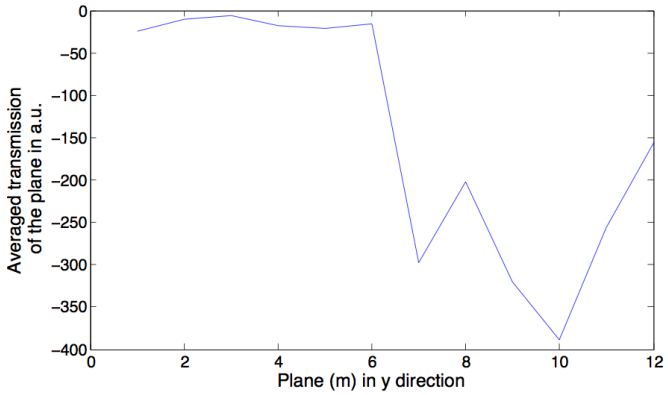

Figure 5.8: Averaged relative transmission values as a function of the plane for the same sample as in Figure 5.7. - The transmission per plane is relatively uniform but drops suddenly after plane 6. The uniformity in Figure 5.7 on the left starts at the same place. The transmission is normalized to the theoretical maximum of that sample.

pling rate on the IR-Spectrometer), a transmission distribution as the one in Figure 8.8, Appendix B is generated, with Figure 8.9, also Appendix B, shows the averaged transmission per plane for these scans. The first illustration (Figure 8.8) proves that a transmission map covering the hole sample without the problem of these uniformities can be obtained by increasing the sampling resolution. However, the second graph (Figure 8.9) reveals that the information of the presence of such a uniformity is lost during this procedure. It is assumed that this is a result of the way the information is recorded and averaged by the IR-Spectrometer. The exact procedures are not publicly documented due to product confidentiality. Therefore, this particular problem will be investigated in further researches and will not be discussed further within the scope of this work. A change in scanning (sampling) resolution for crystals that show this sudden change would also require a rescanning of all other samples with the same resolution to obtain comparable data.

This behaviour was observed for all crystal groups tested and does not seem to be a function of resistivity, because both high and low resistive samples show this behaviour. It was not observed only for the AcroTec samples, which leads to the assumption that these uniformities are possibly connected to the growth technique used by the producer. Then again, the AcroTec crystals are of the highest purity and quality of all the tested

crystals, and an absence of this sudden change does not exclude its existence. Further studies have to be conducted on this topic.

Generally it can be said that this effect is unlikely to be induced by the system, because more than half of all crystals are scanned without this particularity. Furthermore, this uniform part in the transmission maps is recorded on several positions of a sample as top, bottom, middle, etc., but it has not been found for arbitrary angles.

5.4.3 Dynamic Range as a Function of Resistivity

Following the procedure from section 5.3, above and plotting the dynamic range as a function of resistivity, a very interesting aspect is revealed (Figure 5.9). The dynamic range is fluctuating heavily between 10^2 and 10^4 for low resistive crystals, but stabilizes at $1.5 \cdot 10^3$ around $2 \cdot 10^{10}\,\Omega\,m$, which is the same value found by counting Te inclusions with the IRM method. Since the crystals in this graph are ordered by their resistivity (rank in Table 8.2), all samples with a resistivity value above $2 \cdot 10^{10}\,\Omega\,m$ are the same in both methods. A useful fit, as was done in Figure 5.4 to describe the behaviour, could not be found.

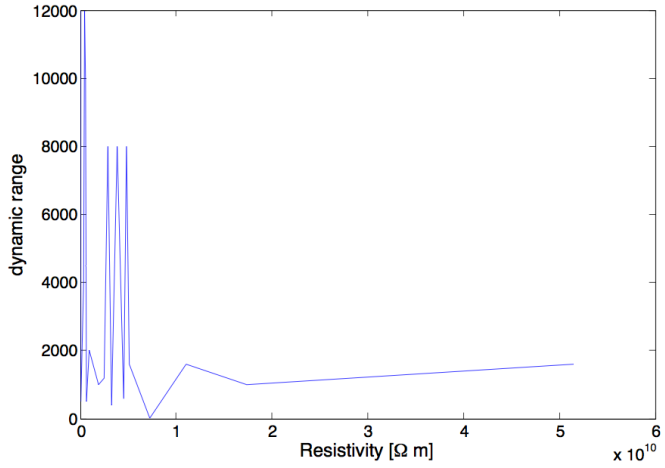

Figure 5.9: The dynamic range of all samples tested as a function of resistivity.
- On the lower end of the $\bar{\rho}$ axis strong fluctuations occur, but stabilize above $2 \cdot 10^{10}\,\Omega\,m$.

5.4.4 Comparison of IRM and IRS

To ensure the highest comparability, the optical test system was designed to obtain data from several test methods simultaneously. The most obvious and interesting aspect is the investigation of a possible connection between the results of the IRM and IRS tests, because both their data are acquired at the same times and positions within a sample. By correlating a transmission with an inclusion (spot) detection map, a combined map as the one in Figure 5.10 is generated. This combined map reveals that there is no connection between high or low transmission areas (dark or white spectra tiles) or the found inclusions at this position. This is due to the fact that the areas of many inclusions ($3 \ldots \geq 6$ - green ... red bubbles) do not only appear at the same positions with the low transmission areas (dark tiles). Conversely, the areas of no inclusions (0 - clear bubbles) do not only appear in high transmission areas (white tiles). For better visualization, the number of found inclusions is plotted as a function of transmission (Figure 5.10). The x-axis (transmission relative to crystal background) was divided into 20 bins and the numbers of found inclusions were summed up in each bin. This procedure leads to a normal distribution of the found inclusions around the relative zero transmission value for that crystal. A connection between the detected inclusions of the IRM method and the relative transmission recorded by the IRS test would shift this distribution to the left. If an image has many Te inclusions, the relative transmission of this area is lower than the same image without these inclusions. Therefore, more spots should be found in areas of less transmission (e.g. dynamic range -300 ... -100), as well as no spots for the positive end of the scale. This is not the case as Figure 5.10 clearly shows. For this reason, a connection of the spectral transmission and the number of inclusions cannot be confirmed. The same applies to the mean (dotted green line) and standard deviation (dotted red lines = $\pm$ 1 σ) of that Figure 5.10. Both would not be gathered around zero, but would be shifted as well. For the sake completeness, a comparison of the distribution of spots as a function of transmission (as in Figure 5.11) has been also done with respect to resistivity. However, no connections could be found here either, only the (spot/ transmission) distribution itself narrows with growing resistivity (and widens with decreasing resistivity). This can be accounted for by to the fact that there are less statistics (overall number of inclusions) to fill the distribution

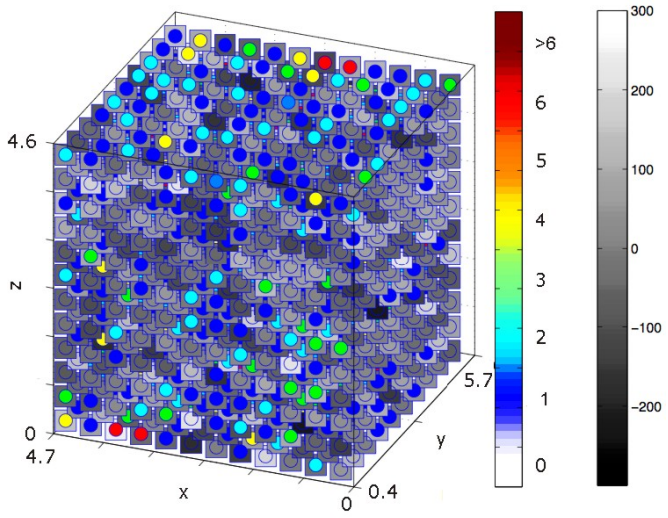

Figure 5.10: Comparison of the 3D maps of IRM and IRS tests of the same crystal. - The number of found Te inclusions is not connected to the colour of the associated spectra tile. The grayscale bar refers to the dynamic range of transmission, while the coloured bar relates to the number of inclusions.

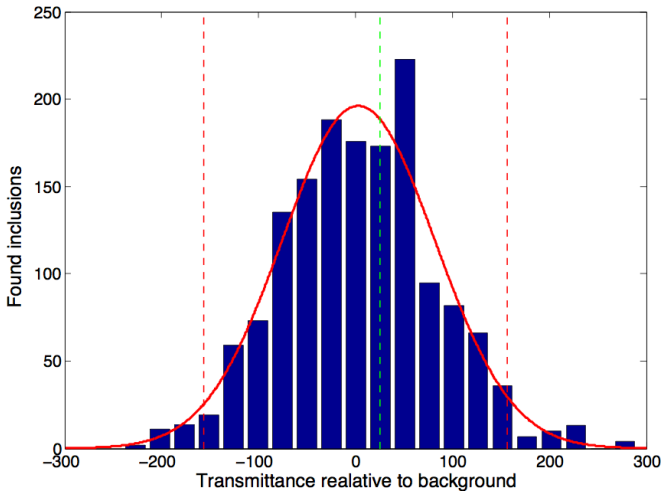

Figure 5.11: Distribution of spots as a function of the relative transmission. - Most inclusions were found at the relative zero transmission (theoretical transmission maximum) of the sample. This confirms that there is no connection between the inclusions distribution and the transmission distribution of a crystal.

for the higher resistive samples than for the lower one. Otherwise, no connection could be found.

5.4.5 High Spatial Resolution Scans

After testing the influence of the scanning resolution (sampling of the spectrometer), the influence of the spatial resolution was tested. For this work, every sample has been scanned with 10 x 12 movement steps per plane and 12 planes. This refers to roughly 433 μm step length (between two scan points) on the x-axis.
This has been increased for the high spatial resolution scan, for the sample *ISCres2_samp1*. The number of steps has been increased and the size of the recorded image decreased to (150 x 100) μm. Possible double counts, due to the smaller step size, were carefully excluded by choosing a size 20 μm longer than the image size. With these measures, the scanned volume could be increased more than 12 times, which is, in numbers of IR-images and spectra, an increase from $2 \cdot 1560$ data points to $2 \cdot 18140$. This leads to a processing time of several days.
A comparison of the obtained data, for example the transmission maps, shows that these vary a lot less for the high spatial scan (Figure 5.12). In addition the dynamic range is lower than for the low resolution scan of the same sample. After scaling the

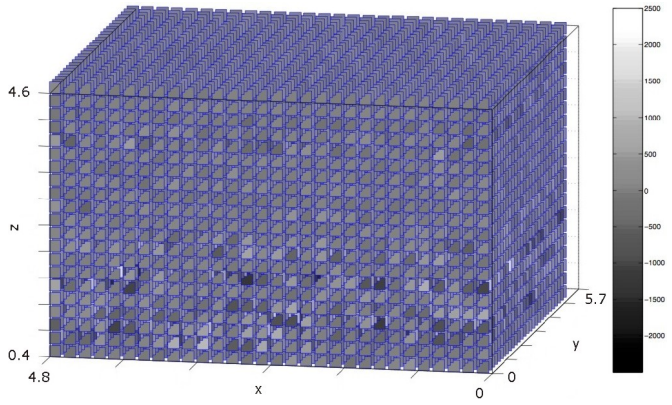

Figure 5.12: High spatial resolution scan of the same crystal as in Figure 8.7. - The varaiation of absorption throughout the crystal is a lot less in the high resolution scan. Also the dynamic range is reduced.

found inclusion of the high resolution scan down to the low resolution one (by dividing the found inclusions through the factor of increased data points), it is revealed that

the number of found inclusions per scanned cubic millimetre[1] is about the same. A

Table 5.2: Stability of found inclusions with increase of the spatial resolution - A comparison of found inclusions (spots) per scanned volume [mm^3] of two different spatial scanning resolutions. The factor [1] between both scans is about the same for the number of data points and found spots. This leads to similar numbers of spots/ mm^3 for both scans. Note: the background files have been removed from the number of data points.

	Low Spatial Resolution	**High Spatial Resolution**
data points	1440	17640
found spots	2010	27425
spots/ scanned volume [mm^{-3}]	20.99	23.39

comparison as seen in Figure 5.11 has also been done for the high spatial scan. The distribution of spots of relative transmission reveals that no significant changes occur by increasing the spatial resolution (Figure 5.13). Such changes, are a completely different shapes of the distribution or an extreme shift to either one of the sides of the transmission's scale. On this account, the high spatial resolution scan can be considered as an option for a highly detailed investigation of a crystal, if the involved testing time (2 weeks for data acquisition and processing) is justified to obtaining better detailed results. The sample itself had not been touched in between the normal resolution scan

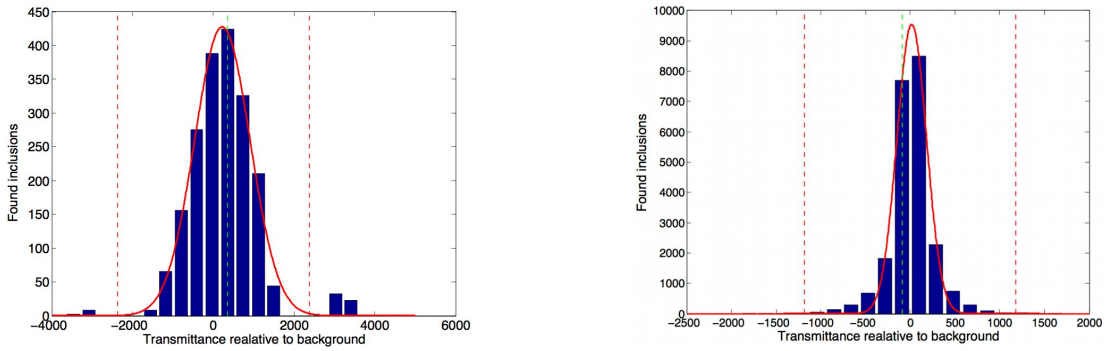

Figure 5.13: Comparison of the spots per transmission plots for a low and high spatial resolutions scan of the same crystal. - The variation of absorption throughout the crystal is a lot less in the high resolution scan (*right*). Also the dynamic range is reduced.

and the high-spatial one. Only the movement script had been altered.

[1]The number of inclusions is 13.64 times larger for the higher resolution scan, while the number of data points increased 12.25 times. The scanned volume is 95.72 μm^3.

5.5 γ- Spectroscopy

Judging from the results of the previous sections, the most reasonable way is to analyse the spectral (γ-) performance of a crystal is with respect to its resistivity.
Unfortunately this is not as straight forward as with the other tests, since the signal of a CZT crystal generated by a γ-source is not only dependent on the crystal itself, but is also strongly dependent on the surface treatment, electrodes, readout system and its adjustment to the unique characteristics (e.g. capacitance) of the crystal. Hence a comparison can only be of qualitative and not quantitative nature.
First, an analysis of samples that produce a readable spectra (Am-241, or Cs-137) independent of their spectra quality will be performed, then a more detailed breakdown of the quality of the spectra. Lastly a distinction between both sources will be made.

5.5.1 Minimum Resistivity to Resolve a Radioactive Spectrum

In this work, a readable spectrum of a radioactive source obtained by a crystal is defined as a spectrum that contains a peak (or a broad bump that can be recognized as a peak) at the approximate position a peak is expected with the used source. According to this definition, a readable spectrum is the one on the *left* in Figure 4.6, while the one on the *right* is considered noise. A good quality spectrum contains clear peaks from which *S/N* ratios can be calculated, while a bad spectrum contains broad bumps (no clear peak), which can hardly be distinguished from the background. Table 5.3 below contains the results of all analysis named in the paragraph above.
A $+$ sign indicates that a spectrum with a clear peak is recorded. The O sign represents the case of a recorded spectrum, but with no clear peak. Finally an *empty cell* indicated that no spectra could be recorded. Special cases like the $*$ represent crystals that have too high a leakage current (several volts after the preamp, no bias voltage applied) that no data could be recorded. The double star $**$ refers to no available data. This is due to a systematic reason. The spectrometer casket provides strong shielding against electromagnetic radiation, but can only shield for bias voltages smaller than 500 V. At 523 V, at least one component produces a high leakage current which makes any further measurement impossible. The big crystal needs a very high bias voltage[1] due to its thickness of 10 mm. The maximal voltage of the spectrometer is still below

[1] $100\,\mathrm{V/mm}$ @ $\bar{\rho} \geq 10^9\ \Omega\,\mathrm{m}$

the minimum depletion voltage of the crystal. This problem will be addressed by an updated version of the casket planned in the second stage of research. Finally the † addresses the special case of the AcroTec crystals, here it has not been possible to record Am-241 spectra due to too high noise. This problem is discussed in section 5.5.2.

Table 5.3: Capability of resolving a signal of radioactive source - The + sign indicates that a signal can be resolved with a clear peak; *O* a signal can be resolved, but the peak is very broad. The lack of resolving a signal is represented by an *empty cell*. Ordered by resistivity, the dashed lines are the separations of the crystal classifications introduced in Chapter 5.3.

Rank	**Sample name**	$\bar{\rho}$ **in** $\Omega\,\mathbf{m}$	**Spectra Am-241**	**Spectra Cs-137**
1	*ISCres1_samp14*	$4.11 \cdot 10^6$		
2	*ISCqual_sampF*	$1.58 \cdot 10^7$	*	*
3	*ISCqual_sampD*	$2.43 \cdot 10^7$	*	*
4	*ISCdope_samp5*	$2.47 \cdot 10^7$	O	
5	*ISCqual_sampC*	$6.52 \cdot 10^7$		
6	*ISC_big*	$3.63 \cdot 10^8$	**	**
7	*ISCetch1_samp4*	$4.33 \cdot 10^8$	O	
8	*ISCqual_sampB*	$5.23 \cdot 10^8$	+	+
9	*ISCetch2_samp2*	$6.20 \cdot 10^8$		
10	*ISCres1_samp6*	$9.50 \cdot 10^8$		
11	*ISCpolish_samp3*	$1.88 \cdot 10^9$	+	O
12	*ISCres2_samp4*	$2.46 \cdot 10^9$	+	+
13	*ISCres2_samp1*	$2.91 \cdot 10^9$	+	+
14	*ISCres2_samp2*	$3.21 \cdot 10^9$	+	+
15	*ISCetch1_samp2*	$3.86 \cdot 10^9$		
16	*ISCqual_sampA*	$4.51 \cdot 10^9$	+	+
17	*ISCdope_samp2*	$4.86 \cdot 10^9$	+	+
18	*ISCetch2_samp3*	$5.06 \cdot 10^9$		
19	*ISCres2_samp3*	$7.25 \cdot 10^9$	+	+
20	*ISCpolish_samp* 2	$1.10 \cdot 10^{10}$	+	+
21	*Acro_8.4*	$1.74 \cdot 10^{10}$	†	+
22	*Acro_8.5*	$5.15 \cdot 10^{10}$	†	+

5.5.2 Detailed Breakdown of Spectra Quality

By visualizing Table 5.3 with respect to the crystal classes suggested by Chapter 5.3, a more clear view is provided.

Only one of the samples of the low quality class produces a readable bump spectrum, while approximately 70 % of the intermediate class crystals produce readable spectra and 100 % of the high quality class. This indicates that the classification introduced in Chapter 5.3 is a solid suggestion.

Judging whether or not a spectra contains a clear peak, the chosen classification is verified further. No sample from the low quality class produced a clear spectra, while 62 % of the second class did. Only the sample *ISCetch1_samp4* with the lowest resistivity in the intermediate class did not meet the criteria. By This means that the classification limit suggested in Chapter 5.3 could be raised to $5 \cdot 10^8$ Ω m for the lower end of the intermediate class. In the high quality class, all samples produced spectra with clear peaks.

The distinction by radioactive sources does not show major differences. Generally more detectors produced spectra with the Am-241 source, while slightly less (11 out of 13) are able to produce Cs-137 spectra. From the lower class, no spectra were produced for either sources, besides *ISCdope_samp5* which produces broad Am spectra. In the intermediate class, the sample ranked 7 was only able to detect Am, while all other sensors detect both sources. In the top class, basically only the sample ranked 20 *ISCpolish_samp2* produced spectra for both sources, while the two AcroTec samples only did for Cs. The surface treatment of these samples is the reason for the absence of Am spectra. These crystals, which are polished but not passivated, have a thin layer [1] of oxidized Te at the surface. This layer of high resistivity absorbs γ-quanta, but does not produce charge carriers that could be absorbed by the electrodes and contribute to a signal. After this layer, the γ-quanta of Am are reduced and the charge carriers produced by the bulk material are too few to significantly stick out of the noise on the recorded spectra. In addition, due to this surface layer, further noise is induced and the signal is further reduced. That this effect only appears for the Am-241, but not for the Cs-137 source, is due to the fact that the γ-energy of the Cs-137 source is 10 times larger than the one of Am. Thus the γ-quanta of Cs-137 penetrate the bulk material of a detector better.
However, judging from the results obtained by the other test methods, it is likely that these samples can provide Am-241 spectra if the proper treatment has been performed.

[1] This is the most likely the interfacial layer found by Bolotnikov, [21]

Synopsis

In this section we have seen that a comparison of the results of each test method to the resistivity is the most useful and reasonable approach for a substantial analysis.

The IRP test as the fastest and simplest method reveals major crystallographic defects such as voids and cracks, and whether or not the sample is processed enough for further optical investigation.
During these tests a 3D inclusion map resulting from the IRM test visualizes the spatial distribution of Cd vacancies represented by Te inclusions within the bulk material. This is very valuable information for improving and understanding the growth process of CT/ CZT, because these spatial distributions can be linked to influenceable growth parameters, such as the temperature or pressure. Furthermore, the results of the IRM test expose a point of significance at $2 \cdot 10^{10}\,\Omega\,\mathrm{m}$. Above this value the number of Te inclusions (and therefore Cd vacancies) converge at a constant value of 5 inclusions/ mm^3. Below this point the number of inclusions significantly increase and are subject to strong variations.
The same result was obtained with the newly introduced IRS method by sorting the crystal's dynamic ranges of transmission as a function of their resistivity. Here again a value of $2 \cdot 10^{10}\,\Omega\,\mathrm{m}$ was found as the point of stabilization, above which the dynamic range converges at a constant value of 1500.
This number, independently found by two different tests, is proposed as a threshold to separate high quality crystals that are usable for spectroscopic purposes and intermediate grade crystals sufficient for detecting applications.
Furthermore, the results of the IRS test indicate that this new test method does not depend on the surface condition of a sample (besides the needed optical transparency - processed until polishing), this makes the IRS scan an excellent method for testing the whole spectrum of defects that are usually found in CT/ CZT detectors.
In addition, a possible connection between the IRM and IRS methods has been investigated. The results clearly suggest that there is no connection between the test methods. Therefore, each one is a test for a different aspect of defects, but both complement one another for a better crystallographic characterization.
Finally, all samples were tested for their performance as a detector of a radioactive signal. Crystals were processed into detectors by chemically applying gold electrodes,

and surface passivation was performed. The results from the γ-test confirm a classification system as suggested in Chapter 5.3. Low quality samples with a resistivity of less then $10^8\,\Omega$m are of no use for any detection purposes, while above this number the γ-detection of at least 60 to 660 keV is possible. Samples with this capability are ranked intermediate. High quality samples, possessing resistivities of at least $2 \cdot 10^{10}\,\Omega\,\mathrm{m}$, are usable for imaging and spectroscopic applications.

This page is intentionally left blank

6

Summary and Prospectus

Within the scope of this work, an automated characterization system for CT/ CZT semiconductor crystals had been developed. This characterization system allows the scanning of a crystal in an early production stage (only cutting, grinding and polishing performed) and roughly predicts its performance as a radiation sensor.
The results obtained by this new system were compared to the of results the standard tests, and commonalities were found.

Starting from optical characterization, a system was developed to integrate several test methods into a single system. Since such a system did not exist, all the needed components were designed and build to fit into the limited compartment space of a tabletop IR-Spectrometer.
For this system, the path of optical characterization had extensively been exploited by integrating three different test methods into one system. Only one of these methods, the infrared panorama observation (IRP), is a common method in industrial production of CT/ CZT detectors. The infrared microscope scan (IRM), mainly used in research, had been further developed into a high resolution 3D mapping test, with its focus on finding tellurium inclusions that relate directly back to the resistivity of a crystal. Due to this circumstance, resistivity estimations can be made with optical data only. In addition, the new system allows the visualization of the spatial distribution of tellurium in a previously unseen resolution. This information is of great value for the growth research of CT/ CZT and will help to better understand the process by connecting the number, position and size of the inclusions with parameters that can be controlled during the growth of the crystals.

One of the major results of this new test method is the suggestion of a three-class quality categorization for CZT crystals by their resistivity. A classification by resistivity is a common procedure, but had not been confirmed with optical data yet.
In addition to this, the results of the IRM method revealed that the distinction between intermediate and upper class crystals is set around $2 \cdot 10^{10}\,\Omega\,\mathrm{m}$. This is a point where the detector's signal is detailed enough to be used for spectroscopic and imaging applications and is the same point at which the stabilization of inclusions/ mm^3 occurs for further growing resistivity.

Of similar value are the results obtained by the newly invented infrared spectroscopic scan (IRS), with which 3D transmission maps, similar to the IRM maps, can be produced. These transmission maps enable the assessment of the submicron tellurium distribution of a crystal, and are a useful source of information to investigate, better understand and explain the material mixing processes during the growth of CT/ CZT.

The results of all the methods were also compared to the in-field performance of the detector crystal, by recording the response signal of a radioactive source. A procedure that further approved the classification system, suggested by the IRM method.

The data of both 3D scanning methods (IRM, IRS) was been compared to the resistivity measured for all samples. Both tests independently point to a value of $2 \cdot 10^{10}\,\Omega\,\mathrm{m}$ at which the attributes (spots/ dynamic range) stabilize towards a constant value. This value (with offset subtracted) is very close to the resistivity needed for spectroscopic applications as referred to by Eisen [22]. Therefore, the choice of $2 \cdot 10^{10}\,\Omega\,\mathrm{m}$ as a minimum resistivity value for spectroscopic grade detectors is further supported.

The aim of finding candidates for an industrial standard revealed that this three-class rating is a possible option for such a standard. Since the results of all test methods (number of inclusions/ mm^3, dynamic range of transmission, FWHM of the γ-test, etc.) can be correlated to the resistivity of a sample, it is most reasonable to follow that approach. The found classification will be discussed with the producers of the crystals used.

Another aim of this work is the development of a database with which the prediction of a crystal's detector performance can be made based on the results obtained by the

characterization in an early production stage. Such a database was initiated and will be extended with more crystals tested. With the little (mainly optical) data available in this database predictions of a detector's performance are already possible. Nevertheless, these only apply to crystals grown under similar conditions as the tested ones had been. These predictions can be improved by including the data of all test methods covered in this work as well as the characterization data of more crystals.

Within the scope of this work, all set goals were achieved. An automated test system for optical characterization of CT/ CZT crystals has been developed, and studies on the comparability of the chosen optical characterization methods with established electronic ones has been conducted. The results obtained from the new methods led to similar conclusions as do the established ones. Additionally, the optical testing is faster, cheaper and more precise than existing tests.
New methods not only open new possibilities of conducting existing processes, but also open new questions to problems that have not occurred before. Therefore, the following aspects should be investigated in additional studies.
First, the investigation and removal of the resistivity offset which might have an influence on the suggested classification system. Second, the origin of the sudden density changes of Te discovered in the IRS-transmission maps and its possible occurrence in crystals produced by other manufacturers. This will increase the statistical diversity and will allow more precise predictions of a detector's performance. Furthermore, the analysis with individual spot detection thresholds, based on the crystal classification needs to be repeated. This will improve the efficiency of this method and provide more precise inclusion numbers needed for the growth research. The integration of the remaining test methods which will allow the acquisition data from all methods in a single run, hence a full-automated test system, is another point that further research should concentrate on. Finally, parts of the existing system can be improved by updating and fine-tuning of the components.

This page is intentionally left blank

References

[1] Dieter K. Schroder. *Semiconductor Material And Device Characterization.* John Wiley & Sons Inc. Hoboken New Jersey (2006) ISBN-13: 978-0-471-73906-5 5, 6

[2] Eugene Hecht. *Optics.* Addison Wesley; 4 edition (August 12, 2001) ISBN-13: 978-0-805-38566-3 7, 8

[3] Wolfgang Demtröder. *Experimentalphysik 2.* Springer-Verlag Berlin Heidelberg New York, 3. Auflage ISBN-10: 3-540-20210-2 7, 10

[4] John Lilley. *Nuclear Physics Principles and Applications.* John Wiley & Sons Inc., Chischester, 1. edition (2001), chapter 7 ISBN-13: 978-0-471-97936-4 73, 76

[5] Glenn F. Knoll. *Radiation Detection and Measurement.* John Wiley & Sons, Inc., 3. edition (2000) ISBN-10: 0-471-07338-5 15, 17, 18, 20

[6] Herman Cember, Thomas E. Johnson. *Introduction to Health Physics.* The McGraw-Hill Companies, 4. edition (2009) ISBN-13: 978-0-071-42308-3 73, 74, 76

[7] Foiles, C. L.: Sn - Zr. Hellwege, K.-H., Olsen, J. L. (ed.). *SpringerMaterials - The Landolt-Börnstein Database.* Landolt-Börnstein Database on Springer materials DOI: 10.1007/10201705_38 11

[8] Foiles, C. L.: Figs. 1 - 26. Hellwege, K.-H., Olsen, J. L. (ed.). *SpringerMaterials - The Landolt-Börnstein Database.* Landolt-Börnstein Database on Springer materials DOI: 10.1007/10201705_39 11

[9] Charra, F., Gurzadyan, G.: P - Z. Nelson, D. F. (ed.). *SpringerMaterials - The Landolt-Börnstein Database.* Landolt-Börnstein Database on Springer materials DOI: 10.1007/10134958_42 11

[10] Gutowski, J., Sebald, K., Voss, T.: $Cd_{1-x}Zn_xTe$: refractive index, absorption, dielectric constants. Roessler, U. (ed.). *SpringerMaterials - The Landolt-Börnstein Database.* Landolt-Börnstein Database on Springer-Verlag Berlin Heidelberg, 2008 DOI: 10.1007/978-3-540-74392-7_101 12

[11] S. Sen, et al. *Infrared Absorption Behavior in CdZnTe Substrates.* J. Electron. Mater., Vol. 30, No. 6, 611-618, year 2001 12, 29

[12] G. A. Carini, et al. *Material Quality Characterization of CdZnTe Substrates for HgCdTe Epitaxy.* J. Electron. Mater., Vol. 35, No. 6, 1495-1502, year 2006 12, 29

[13] Y. Cui, et al. *CZT Virtual Frisch-grid Detector: Principles and Applications.* BNL-82046-2009-CP, January 2009 22

[14] Loferski, Joseph J. *Infrared Optical Properties of Single Crystals of Tellurium.* DOI: 10.1103/PhysRev.93.707 Physical Review, Vol. 93, No. 6, 707-716, year 1954 11

[15] Ezzat S., et al. *Correlation of tellurium inclusions and carrier lifetime in detector grade cadmium zinc telluride.* Applied Physical Letters, 93, 042112, year 2008 27, 29, 35

[16] Muren Chu, et al. *Role of Zinc in CdZnTe Radiation Detectors.* IEEE Transaction of nuclear science, Vol. 51, No. 5, 2405-2411, October 2004 12

REFERENCES

[17] A. Cola, et al. *Electric Field Properties of CdTe Nuclear Detectors.* IEEE Transaction of nuclear science, Vol. 54, No. 3, 868-872, August 2007 34

[18] C.J. Sullivan, et al. *Bulk Uniformity of Cadmium Zinc Telluride (CZT) Crystals for Large Volume Coplanar Gamma Spectrometers.* IEEE Nuclear Science Symposium Conference Record, N27-4, 1805-1808, 2007 34

[19] P. De Antonis, et al. *Measuring the bulk resistivity of CdZnTe single crystal detectors using a contactless alternating electric field method.* IEEE Nuclear Instruments and Methods in Physics Research A, 380, 157-159, 1996 35

[20] Stefano Del Sordo, et al. *Progress in the Development of CdTe and CdZnTe Semiconductor Radiation Detectors for Astrophysical and Medical Applications.* Sensors 2009, 9, 3491-3526, 12 May 2009 DOI: 10.3390/ s90503491 20

[21] Aleksey E. Bolotnikov, et al. *Properties of Pt Schottky type contacts on high-resistivity CdZnTe detectors.* Nuclear Instruments and Methods in Physics Research A 482, 395407, 2002 46, 63

[22] Y. Eisen, et al. *CdTe and CdZnTe gamma ray detectors for medical and industrial imaging systems.* Nuclear Instruments and Methods in Physics Research A 428, 158-170, 1999 68

[23] Lect. PhD Kenneth Österberg. *Accelerator And Experiments in High Energy Physics.* Helsinki Institute of Physics Lecture script, fall 2008 16

[24] Prof. Friedhelm Bechstedt. *Einführung in de Festkörperphysik.* Institut für Festkörpertheorie und Theoretische Optik Lecture script, winter semester 2007/ 2008 11, 14

[25] Radiation and Nuclear Safety Authority Finland, 20.04.2011 74, 76

[26] Radiation handling rules of the University of Nottingham, 20.04.2011 75, 76

[27] Radiation protection on Wikipedia. 76

[28] Wikipedia image used to explain forward biased *pn*-junctions. 19

[29] Wikipedia image used to explain reversed biased *pn*-junctions. 20

[30] Data sheet of Feinmess MP63 stage, 25.04.2011. 28

[31] Data sheet of polarizer: colorPol ®IR 1300 BC5, 25.04.2011. 42

[32] Transmission spectra of ZnSe, 25.04.2011. 42

[33] Data sheet of the Canberra Model 2004 preamplifier, 08.05.2011. 32

[34] Data sheet of the AmpTek A250CF preamplifier, 08.05.2011. 32

[35] Institute for Single Crystals, of the National Academy of Sciences of Ukraine, 29.04.2011. 2, 38, 47

[36] AcroTec as part of JX Nippon Mining & Metals, 29.04.2011. 47

7

APPENDIX A - Radiation and Safety

7.1 Handling Radioactive Material

To cover the topic of handling radioactive material would well exceed the size of this work. Many books have been published dealing only with this topic. Which is why this subject will only be touched briefly and referred for further literature of more information.

7.1.1 General

The effect of radioactive radiation on humans is a very complicated function. Kind of radiation, its energy, time and area of exposure (e.g. partially, whole body, organs, bones, internal, external), oxygen state of the tissue, phase of the cell cycle and many more factors are influencing the function of interaction with humans.
With some approximations the following formula can provide roughly the amount of energy deposit by radioactive radiation in tissue. For more detailed information see [4]. The amount of ionizing energy (called *dose* - D - [Gy][1]) deposit per unit time t is called dose rate and is usually given in microsievert per hour, equation (7.1).

$$\frac{d}{dt}\,\mathrm{D} = \frac{\mathrm{Gy}}{\mathrm{t}},\ \text{in} \quad \left[\frac{\mu\mathrm{Sv}}{\mathrm{h}}\right] \tag{7.1}$$

[1] Gy - *gray* is the absorbed radiation dose of one joule per kilogram [6]. $1\,\mathrm{Gy} = 1\ \frac{J}{kg}$

And the approximated energy deposit in tissue per unit time is

$$\mathrm{D} \approx \sum_{\mathrm{i}=1}^{\mathrm{n}} \frac{\xi \cdot (\alpha_{\mathrm{i}}\, E_{\gamma,\mathrm{i}})}{6 \cdot r^2} \tag{7.2}$$

while r is the distance in meters, ξ number of photons in MBq[1] and E_γ the energy emitted by the source in MeV. The geometric factor *6* results from the fraction of the solid angle that will only hit the person. Because the radiation of an unshielded source is spreading spherically. Additionally the sum takes the fact into account that a source usually emits radiation of different energies $E_{\gamma,i}$ and strengths α_i. The dose is equal for X- and γ-rays and is given in unit sievert (Sv). $1\,\mathrm{Sv} \doteq 1\,\mathrm{Gy} = 1\,\mathrm{J\,kg^{-1}}$ Higher energetic emissions such as α radiations are blocked at the source (or at the latest by the skin) that these do not have to be accounted for here.
By these means the estimated dose rate absorbed by a human working with a Cs-137 source of the activity of 3.41 μCi[2], directly facing him in 1 m distance is approximately

$$\frac{0.13\,\mathrm{MBq} \cdot (0.01 \cdot 0.036 + 0.06 \cdot 0.032 + 0.85 \cdot 0.662)\,\mathrm{MeV}}{6 \cdot 1\,\mathrm{m}^2} = 12.22\,\mathrm{nSv/h} \tag{7.3}$$

assuming that the cloth will not absorb any of the radiation. This value is negligible in comparison to the average background radiation which is usually at least ten times higher (Helsinki: 0.14μSv/h [25]).
In comparison a 1 h flight in an air plane at 10 km height will lead to a dose of $\approx$ 1.6 μSv/ h of cosmic radiation, which is the reason why the annual in-the-air working hours of flight personal is restricted.
Nevertheless, relation (7.2) provides an estimation of the risk one has to take into account when working with radiation.
The dose rate for the used Am-241 source is about 4.5 nSv/h (all major γ-emissions), which is even lower and falls below the hourly background fluctuation. Therefore, this source is accepted to be used in common products such as ionizing smoke detectors. Nevertheless, rules of conduct as described in the next section have to be followed.

According to equation (7.2) distance is influencing the dose rate and therefore the

[1] Bq - *becquerel* is the quantity of the number of radioactive decays within a given time. 1 Bq = 1/s [6].

[2] Ci - *Curie* a more historical unit for the activity, but still used to mark the sources. 1 Ci = $3.7 \cdot 10^{10}$ Bq

absorbed radiation the most. On this account increasing the distance to the source to 2 m will reduce D to one quarter.
From equation (7.2) and (many other formulas) safety-rules for radiation protection can be derived.

7.1.2 Security and Conduct

These safety rules can be summarized into the *"Ten golden rules for working with Radiation"* as it has been done by University of Nottingham [26], where these rules have been taken form. Following these advices accidental irradiation of humans can be avoided.

1. Understand the nature of the hazard and get practical training.
   Never work with unprotected cuts or breaks in the skin, particularly on the hands or forearms. Never use any mouth-operated equipment in any area where unsealed radioactive material is used (because of the higher contamination risk inside the body). Always store compounds under the conditions recommended. Label all containers clearly, indicating nuclide, compound, specific activity, total activity, date, and name of user. Containers should be properly sealed.

2. Plan ahead to minimize time spent handling radioactivity.
   Carry out a "dummy run" without radioactivity to check your procedures. (The shorter the time, the smaller the dose.)

3. Distance yourself appropriately from sources of radiation.
   Doubling the distance from the source quarters the radiation dose (The Inverse Square Law).

4. Use appropriate shielding for the type of radiation.
   1 cm Perspex/Plexiglas will stop all beta particles but it is important to be aware of Bremsstrahlung from high-energy beta-emitters. Use suitable thickness of lead or lead acrylic shielding for X-ray and gamma-emitters.

5. Contain radioactive materials within defined work areas.
   Always keep active and inactive work separated as far as possible, preferably by maintainning rooms used solely for radioactive work. Always work over a spill tray within a ventilated enclosure. These rules may be relaxed for small (a few tens of kBq) quantities of ^{3}H-, ^{35}S-, ^{33}P-, ^{14}C-, and ^{125}I-labelled compounds in a non-volatile form in solution.

6. Wear appropriate protective clothing and dosimeters.

   Laboratory overalls, safety glasses, and surgical gloves must be worn at all times. However, beware of static charge on gloves when handling fine powders. Local rules will define which dosimeters should be worn (e.g. body film badge or thermoluminescent extremity dosimeter for work with high energy beta-emitters, etc).

7. Monitor the work area frequently for contamination.
   In the event of a spill follow the prepared contingency plan:

   - *Verbally warn all people in the vicinity.*
   - *Restrict unnecessary movement into and through the area.*
   - *Report the spill to the Radiation Protection Supervisor/Adviser.*
   - *Treat contaminated personnel first.*
   - *Follow clean-up protocol.*

8. Follow the local rules and safe ways of working.

   Do not eat, drink, smoke, or apply cosmetics in an area where unsealed radioactive substances are handled. Use paper wipes and dispose of them appropriately. Never pipette radioactive solutions by mouth. Always work carefully and tidily.

9. Minimize accumulation of waste and dispose of it by appropriate routes.

   Use the minimum quantity of radioactivity needed for the investigation. Disposal of all radioactive waste is subject to statutory control. Be aware of the requirements and use only authorized routes of disposal.

10. After completion of work, monitor yourself, wash and monitor again.

    Never forget to do this. Report to the local supervisor if contamination is found.

In a laboratory environment it is possible that some of these rules are not applying, due to the used sources for example. However, because of the danger of radiation it is always good to know these rules to avoid any unneeded exposure and to save lives.
More information can be obtained from books like [4, 6] and webpages such as STUK [25], [26] or [27]. Regardless of any source of information the first contact should always be the authorised *Radiation Safety Officer* of the lab.

8

APPENDIX B - Figures and Tables

8.1 Tables

Table 8.1: Table of defects - Overview of most occurring defects in $Cd_{1-x}Zn_xTe$ crystals. Ordered by increasing significance: − minor, O intermediate, + major; Roman numbers: I - point, II - line, III - planar lattice defect.

#	Name	Crystallographic defect	Example	Description	Significance	Occurrence
1	precipitates/ inclusions	I, III	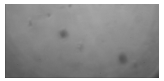	n/ μm sized Cd vacancies, or vacancy complexes; filled with condensations of Te or dopants; all geometric shapes	-	++
2	Te distribution imbalances	I, II, III	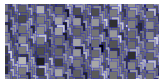	inhomogeneities of Te distribution; can be a local or spread over the whole ingot	-	++
3	scratches	III	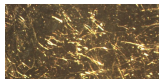	surface damages, several μm deep, usually caused by handling	O	+
4	lattice folds	III	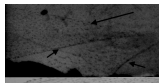	folds in crystals lattice, extra layers	O	-
5	bubble chains	II, III		frozen gas bubbles of few μm size	O	O
6	prolonged voids	III		gas bubbles of μm/ mm sizes	+	-
7	grain boundaries	II, III		boundary between two single crystals (defect distance $\gg$ latice parameters)	+	O
8	cracks	III	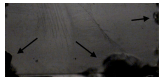	broken lattice over many layers, up to mm size	+	-

Table 8.2: Full table of resistivity $\bar{\rho}$ for all tested crystals - Ordered by groups and within these by $\bar{\rho}$; the error is $\Delta\bar{\rho}$ and the maximal resistivity is given by ρ_{max}.

Group	**Sample Name**	$\bar{\rho}$ **in** $[\Omega\,\mathrm{m}]$	ρ_{max} **in** $[\Omega\,\mathrm{m}]$	$\Delta\bar{\rho}$ **in** $[\Omega\,\mathrm{m}]$	**Rank**
Polishing	*ISCpolish_samp3*	$1.88 \cdot 10^{9}$	$2.11 \cdot 10^{10}$	$8.67 \cdot 10^{7}$	11
Polishing	*ISCpolish_samp2*	$1.10 \cdot 10^{10}$	$4.37 \cdot 10^{11}$	$7.75 \cdot 10^{8}$	20
Etching I	*ISCetch1_samp4*	$4.33 \cdot 10^{8}$	$9.22 \cdot 10^{9}$	$3.49 \cdot 10^{7}$	7
Etching I	*ISCetch1_samp2*	$3.86 \cdot 10^{9}$	$7.91 \cdot 10^{10}$	$3.45 \cdot 10^{8}$	15
Etching II	*ISCetch2_samp2*	$6.20 \cdot 10^{8}$	$9.44 \cdot 10^{9}$	$5.45 \cdot 10^{7}$	9
Etching II	*ISCetch2_samp3*	$5.06 \cdot 10^{9}$	$8.77 \cdot 10^{10}$	$4.31 \cdot 10^{8}$	18
Doping	*ISCdope_samp5*	$2.47 \cdot 10^{7}$	$3.04 \cdot 10^{7}$	$1.62 \cdot 10^{6}$	4
Doping	*ISCdope_samp2*	$4.86 \cdot 10^{9}$	$7.91 \cdot 10^{10}$	$3.18 \cdot 10^{8}$	17
Quality	*ISCqual_sampF*	$1.58 \cdot 10^{7}$	$9.65 \cdot 10^{7}$	$1.20 \cdot 10^{6}$	2
Quality	*ISCqual_sampD*	$2.43 \cdot 10^{7}$	$2.74 \cdot 10^{7}$	$1.64 \cdot 10^{6}$	3
Quality	*ISCqual_sampC*	$6.52 \cdot 10^{7}$	$8.80 \cdot 10^{7}$	$8.80 \cdot 10^{7}$	5
Quality	*ISCqual_sampB*	$5.23 \cdot 10^{8}$	$1.15 \cdot 10^{9}$	$3.49 \cdot 10^{7}$	8
Quality	*ISCqual_sampA*	$4.51 \cdot 10^{9}$	$4.23 \cdot 10^{9}$	$2.95 \cdot 10^{8}$	16
Resistivity	*res1_samp14*	$4.11 \cdot 10^{6}$	$6.10 \cdot 10^{6}$	$3.73 \cdot 10^{5}$	1
Resistivity	*res1_samp6*	$9.5 \cdot 10^{8}$	$4.33 \cdot 10^{10}$	$7.75 \cdot 10^{7}$	10
Resistivity	*res2_samp4*	$2.46 \cdot 10^{9}$	$2.73 \cdot 10^{10}$	$1.61 \cdot 10^{8}$	12
Resistivity	*res2_samp1*	$2.91 \cdot 10^{9}$	$2.17 \cdot 10^{10}$	$2.38 \cdot 10^{8}$	13
Resistivity	*res2_samp2*	$3.21 \cdot 10^{9}$	$3.89 \cdot 10^{10}$	$1.54 \cdot 10^{8}$	14
Resistivity	*res2_samp3*	$7.25 \cdot 10^{9}$	$1.42 \cdot 10^{11}$	$4.65 \cdot 10^{8}$	19
Big	*ISC_big*	$3.63 \cdot 10^{8}$	$3.04 \cdot 10^{9}$	$1.85 \cdot 10^{7}$	6
AcroTec	*Acro8*.4	$1.74 \cdot 10^{10}$	$1.58 \cdot 10^{11}$	$2.92 \cdot 10^{9}$	21
AcroTec	*Acro8*.5	$5.15 \cdot 10^{10}$	$4.70 \cdot 10^{11}$	$8.66 \cdot 10^{9}$	22

8.2 Figures

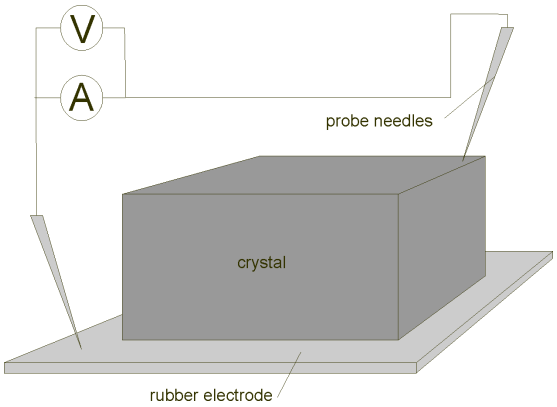

Figure 8.1: Schematics of the electrodes position during a 2-probe measurement. - The figure shows an equivalent schematics view of the used electrode configuration during a resistivity measurement.

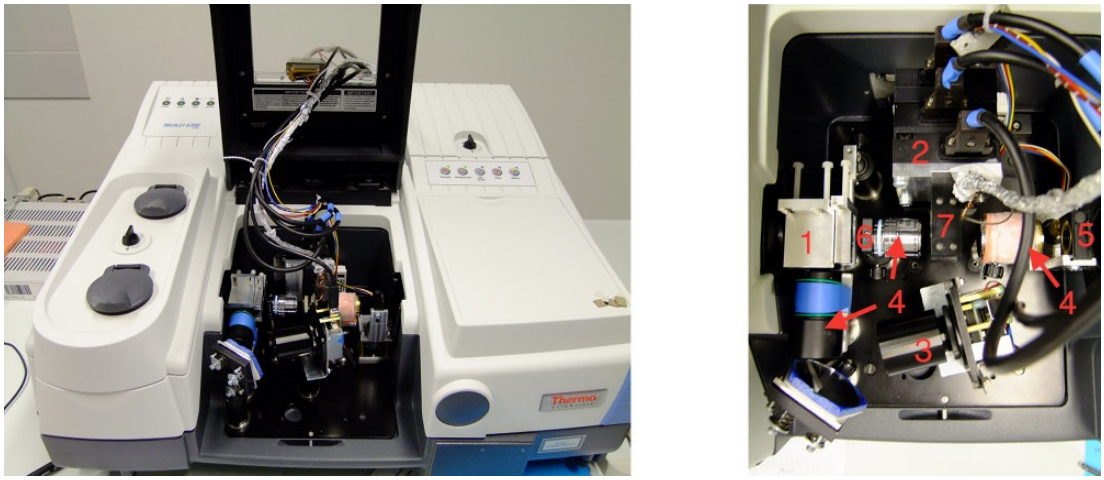

Figure 8.2: A photography of the developed characterization system after the first stage of research. - The figure on the *left* shows the integrated set up in the IR-Spectrometer (white device). The image on the *right* is the actual set up. *1* - beam splitter, *2 - micrometer stage, 3 - CCD camera, 4 - microscope*, *5* - polarizator, *6* - analyzer, *7* - crystal holder, with rubber electrodes.

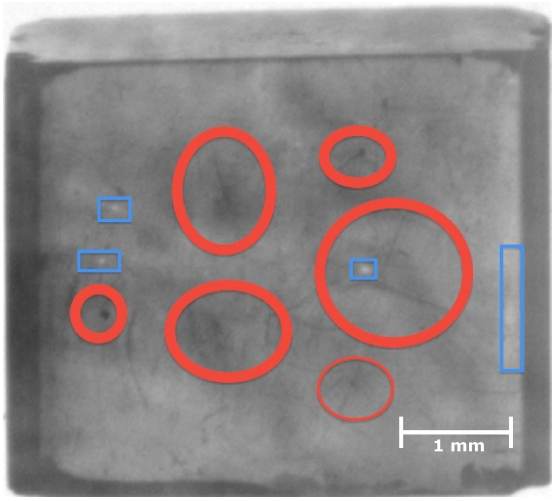

Figure 8.3: IRP image of a sample with some crystallographic defects. - Orange circles mark some of the identified flaws such as scratches and inclusions, while the blue boxes mark background induced flaws like white dots. Image had been enhanced to better visualize the defects.

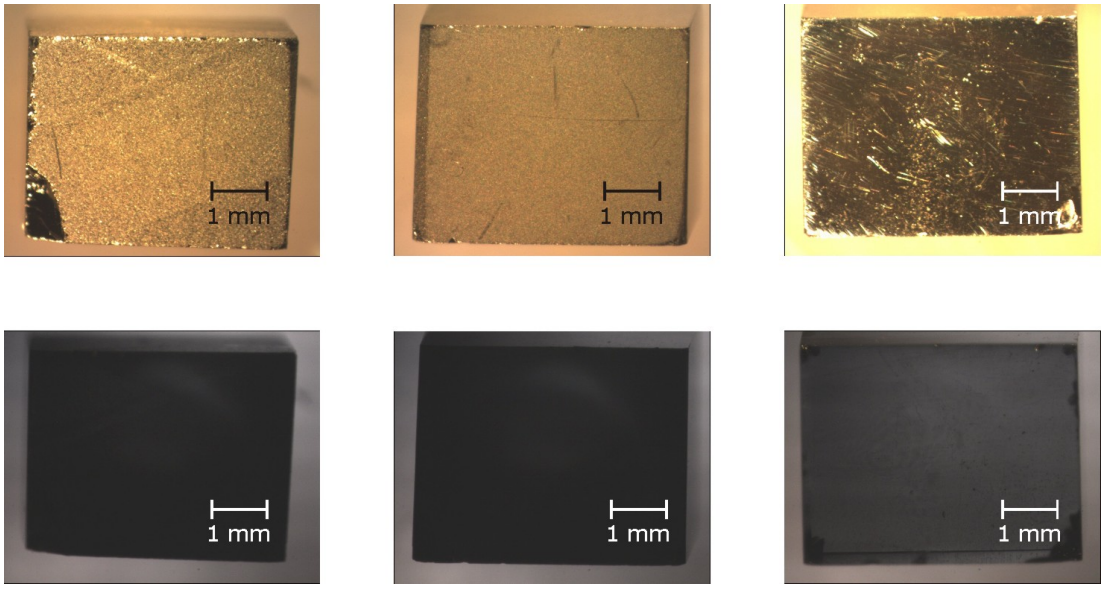

Figure 8.4: IR-transparency during the first processing steps. - The first two process steps cutting (*left*) and grinding (*middle*) leave a too high surface roughness that the IR-light is scattered away. The sample appears black on such an image (second row). Only the third process step (*right*) reveals the wanted behaviour.

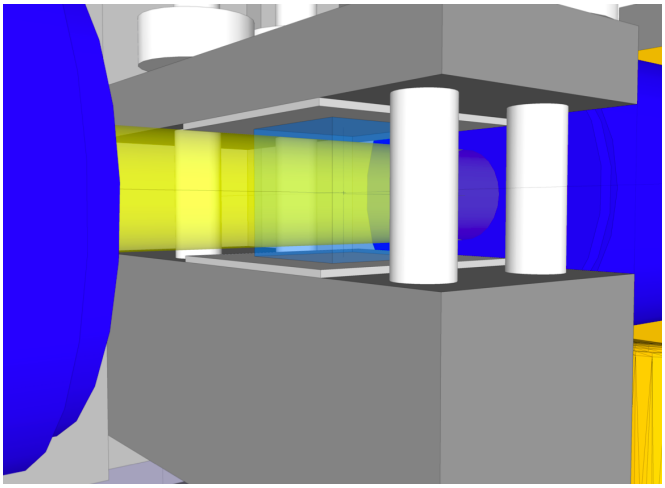

Figure 8.5: CAD-drawing of the crystal holder with rubber electrodes. - The rubber electrodes are visualized by the gray squares above and below the crystal (transparent, blue cube), the yellow bar represents the path of light and the dark gray cuboids with the white rods are the remaining parts of the stage.

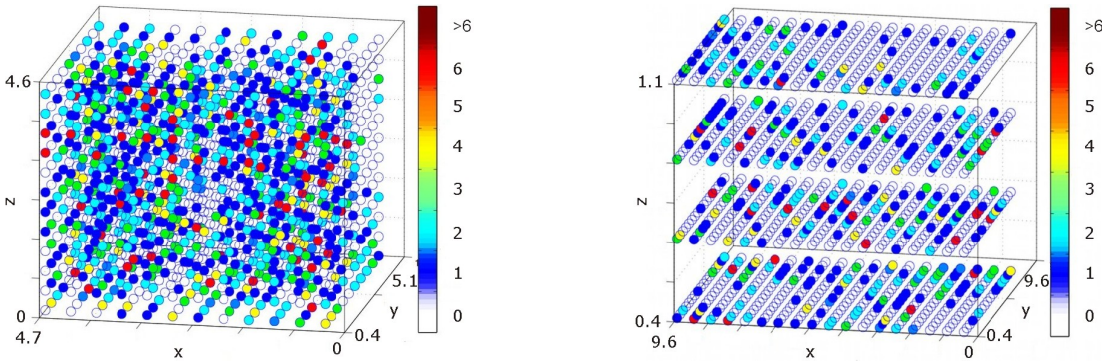

Figure 8.6: Comparison of the inclusion detection map for a low and high resistive crystal. - The free path for a charge carrier, until hitting an area of inclusion, is longer for the *left* sample than for the *right* one.

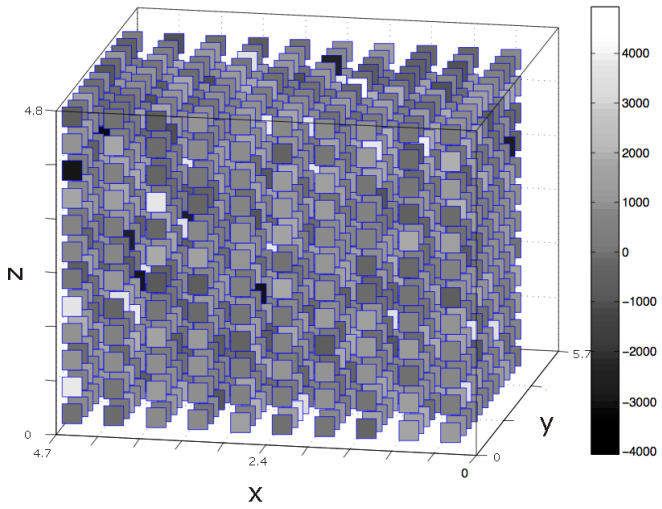

Figure 8.7: A 3D transmission map of a CZT crystal. - The colors of the gray tiles are relatively uniform which refers to a uniform distribution of Te in this sample. The axes *x, y, z* are in mm.

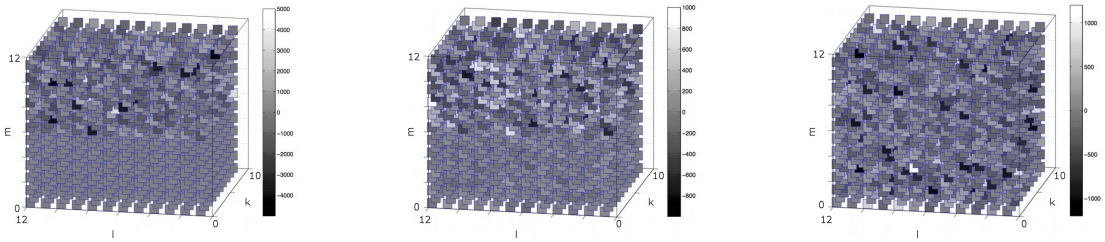

Figure 8.8: IRS scan in 3 different sampling resolutions of the same crystal as in Figure 5.7. - Low - medium - high, from *left* to *right*. The uniformity decreases as does the dynamic range. Note: the axes are labelled in *k, l, m* which refer to the coordinate system within the crystal. The scanned volume is $(4.3 \,\mathrm{x}\, 5.3 \,\mathrm{x}\, 4.2)$ mm in *x, y, z* direction.

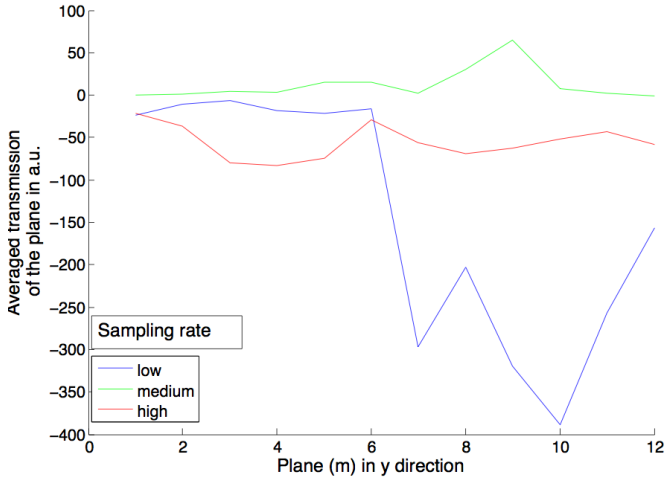

Figure 8.9: Corresponding transmission averaged per plane of Figure 8.8 - The higher sampling rate of the IR-Spectrometer allows to obtain spectra maps without uniform areas, but the information about the presence of such areas is lost.

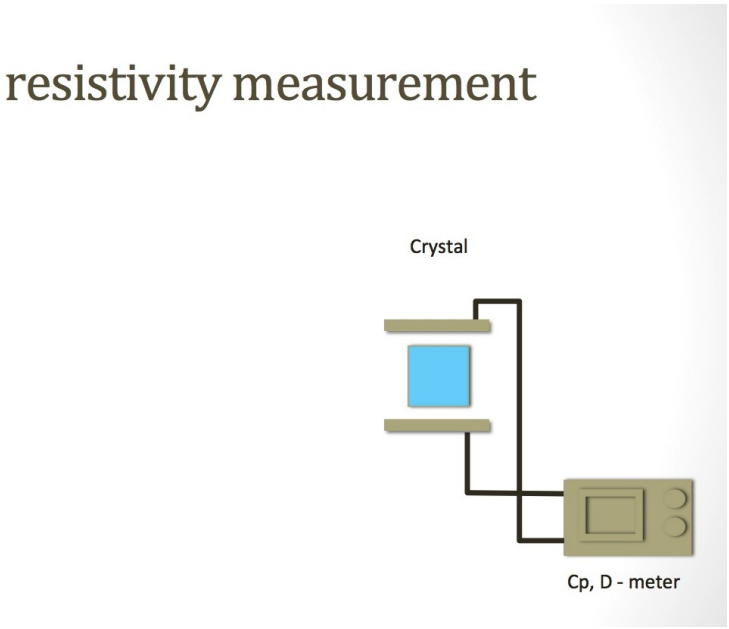

Figure 8.10: Contactless resistivity test -

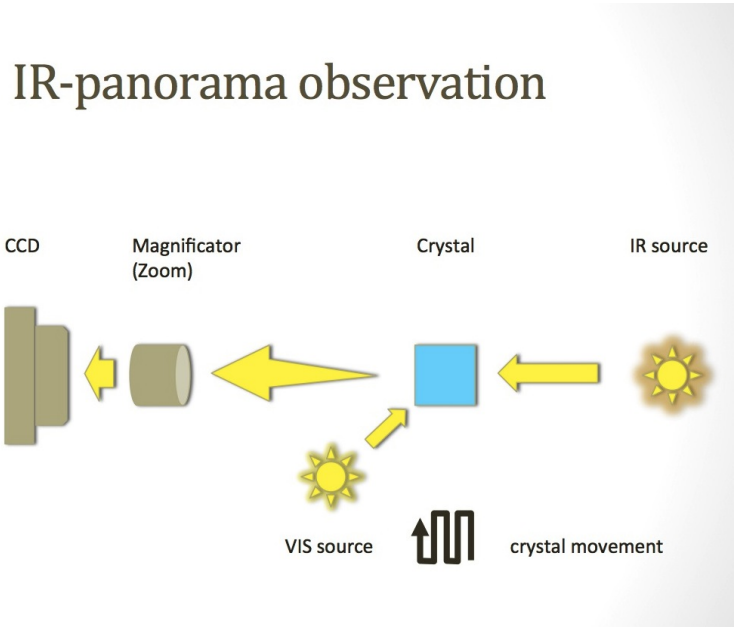

Figure 8.11: IR-panorama observation -

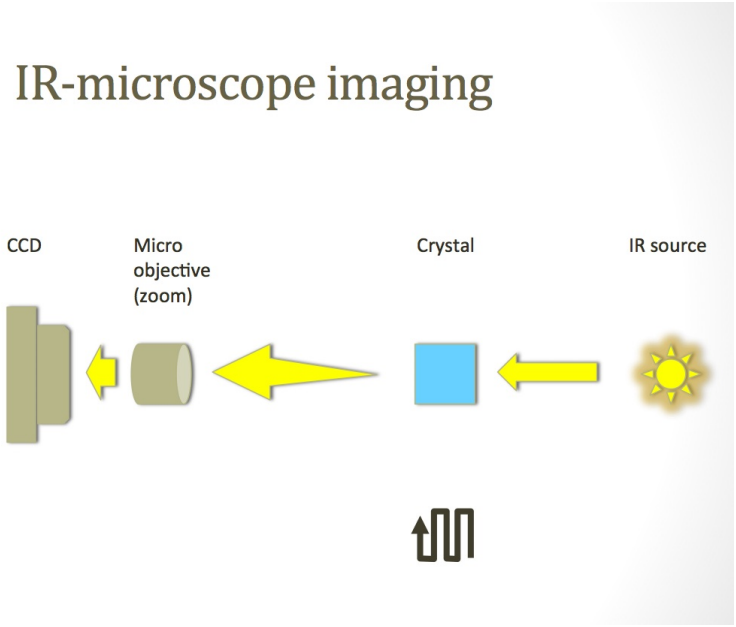

Figure 8.12: IR-microscope scan -

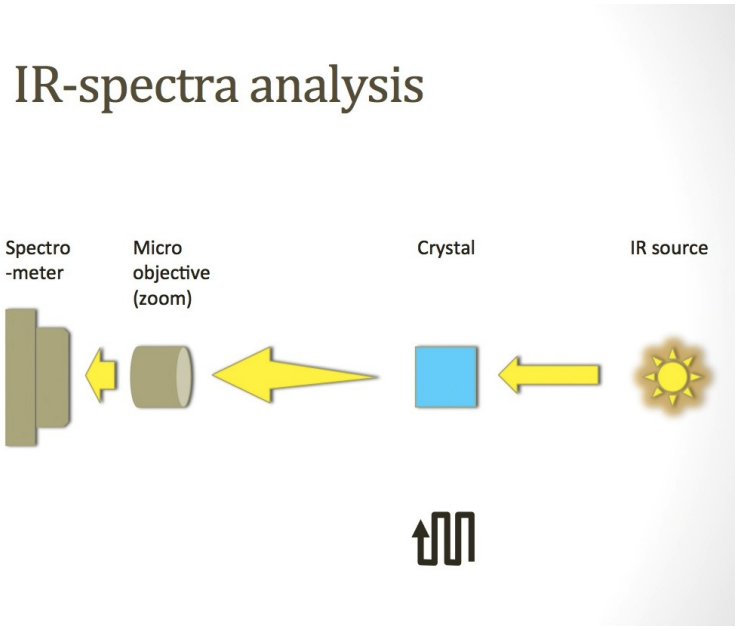

Figure 8.13: IR-Spectrometer scan -

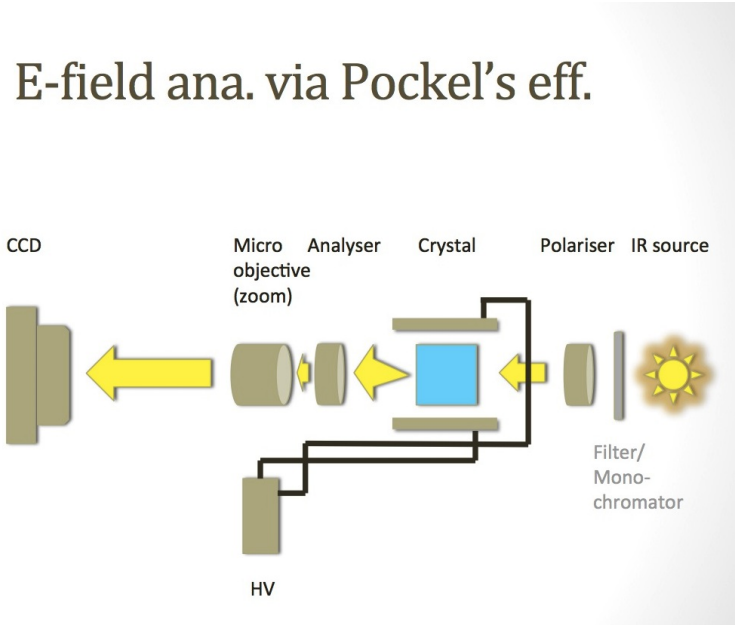

Figure 8.14: Electrical field analysis via Pockel's effect -

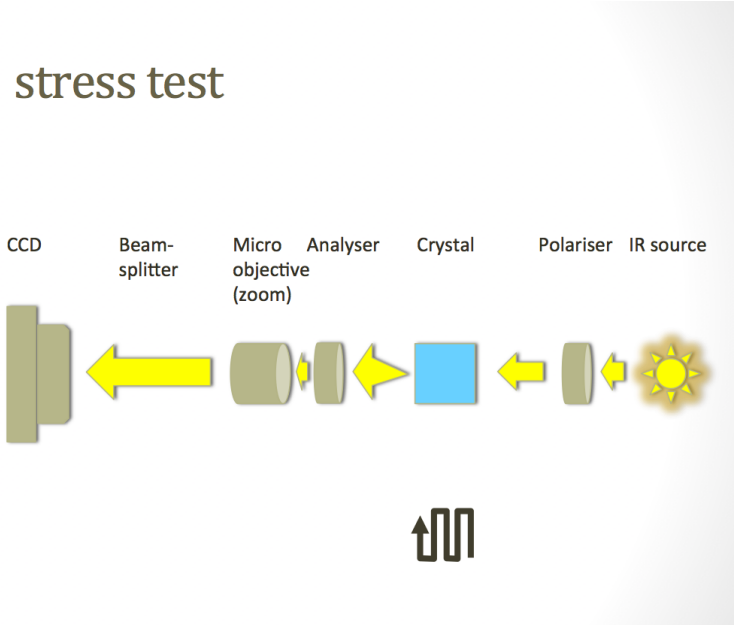

Figure 8.15: Internal stress test -

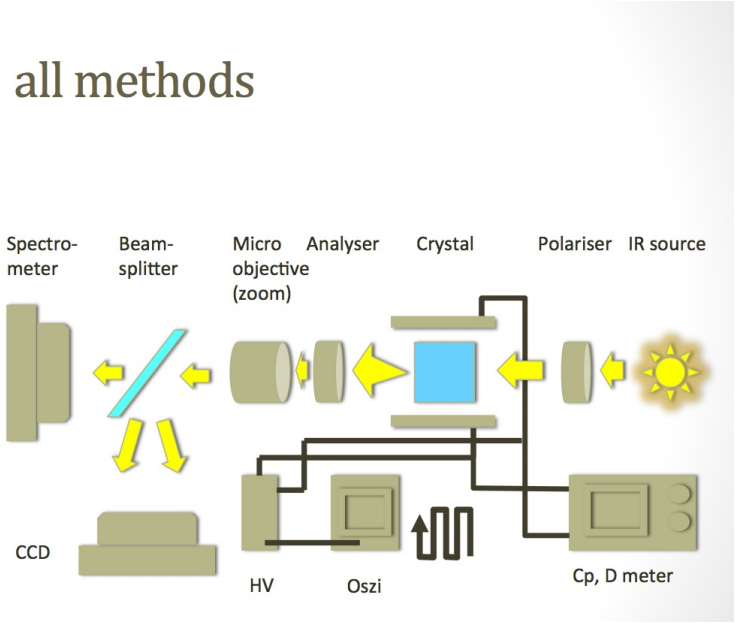

Figure 8.16: Illustration of the integration of all test methods into one test system. - All components have been realized in the final set up (see Figure 8.2) for this work already. However, not all external components were available at the time.

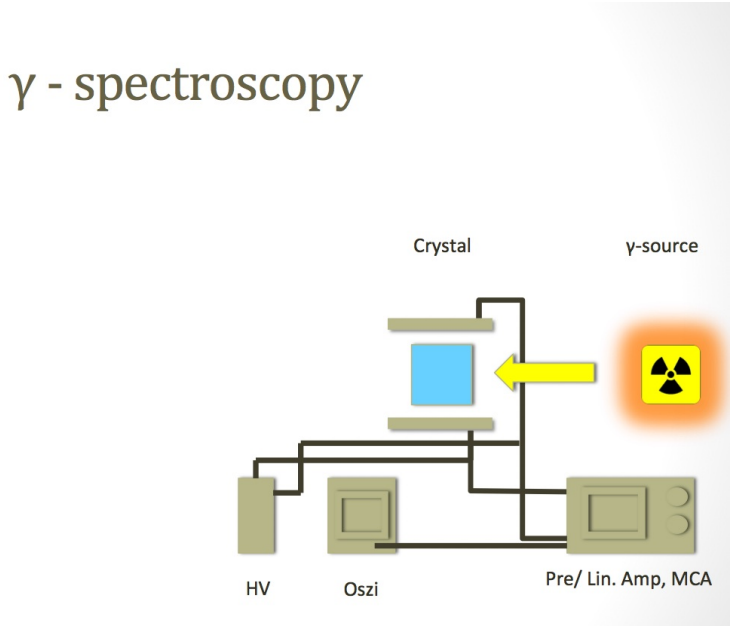

Figure 8.17: γ-Spectrometer - This test has not been included into the final system due to safety reasons. However, an integration is possible.

Declaration

I herewith declare that I have produced this paper without the prohibited assistance of third parties and without making use of aids other than those specified; notions taken over directly or indirectly from other sources have been identified as such.

The work was conducted from 01.03.2010 to 26.05.2011 under the supervision of Tom Schulman at Sensor Center Ltd. and the University of Helsinki.

....

Place, Date Alexander Dieter Winkler

Erklärung

Ich erkläre, dass ich die vorliegende Arbeit selbständig verfasst und keine anderen als die angegebenen Quellen und Hilfsmittel benutzt habe.

....

Ort, Abgabedatum Alexander Dieter Winkler

Seitens des Verfassers/Verfasserin bestehen keine Einwände, die vorliegende Diplomarbeit fur die öffentliche Nutzung in der Thüringer Universitäts- und Landesbibliothek zur Verfügung zu stellen.

....

Ort, Abgabedatum Alexander Dieter Winkler